Magnon spin transport driven by the magnon chemical potential in a magnetic insulator

L. J. Cornelissen,[1,*] K. J. H. Peters,[2] G. E. W. Bauer,[3,4] R. A. Duine,[2,5] and B. J. van Wees[1]

[1]*Physics of Nanodevices, Zernike Institute for Advanced Materials, University of Groningen,*
Nijenborgh 4, 9747 AG Groningen, The Netherlands
[2]*Institute for Theoretical Physics and Center for Extreme Matter and Emergent Phenomena, Utrecht University,*
Leuvenlaan 4, 3584 CE Utrecht, The Netherlands
[3]*Institute for Materials Research and WPI-AIMR, Tohoku University, Sendai, Japan*
[4]*Kavli Institute of NanoScience, Delft University of Technology, Delft, The Netherlands*
[5]*Department of Applied Physics, Eindhoven University of Technology, PO Box 513, 5600 MB Eindhoven, The Netherlands*

We develop a linear-response transport theory of diffusive spin and heat transport by magnons in magnetic insulators with metallic contacts. The magnons are described by a position-dependent temperature and chemical potential that are governed by diffusion equations with characteristic relaxation lengths. Proceeding from a linearized Boltzmann equation, we derive expressions for length scales and transport coefficients. For yttrium iron garnet (YIG) at room temperature we find that long-range transport is dominated by the magnon chemical potential. We compare the model's results with recent experiments on YIG with Pt contacts [L. J. Cornelissen *et al.*, Nat. Phys. **11**, 1022 (2015)] and extract a magnon spin conductivity of $\sigma_m = 5 \times 10^5$ S/m. Our results for the spin Seebeck coefficient in YIG agree with published experiments. We conclude that the magnon chemical potential is an essential ingredient for energy and spin transport in magnetic insulators.

I. INTRODUCTION

The physics of diffusive magnon transport in magnetic insulators, first investigated by Sanders and Walton [1], has been a major topic in spin caloritronics since the discovery of the spin Seebeck effect (SSE) in YIG|Pt bilayers [2–4]. This transverse voltage generated in platinum contacts to insulating ferromagnets under a temperature gradient can be explained by thermal spin pumping caused by a temperature difference between magnons in the ferromagnet and electrons in the platinum [4–7]. The magnons and phonons in the bulk ferromagnet are considered as two weakly interacting subsystems, each with their own temperature [1]. Hoffman *et al.* explained the spin Seebeck effect in terms of the stochastic Landau-Lifshitz-Gilbert equation with a noise term that follows the phonon temperature [8].

Recently, diffusive magnon spin transport over large distances has been observed in yttrium iron garnet (YIG) that was driven either electrically [9,10], thermally [9], or optically [11]. Notably, our observation of electrically driven magnon spin transport was recently confirmed in a Pt|YIG|Pt trilayer geometry [12,13]. Here, we argue that previous theories cannot explain these observations, and therefore do not capture the complete physics of magnon transport in magnetic insulators. We present arguments in favor of a nonequilibrium magnon chemical potential and work out the consequences for the interpretation of experiments.

Magnons are the elementary excitations of the magnetic order parameter. Their quantum mechanical creation and annihilation operators fulfill the boson commutation relations as long as their number is sufficiently small. Just like photons and phonons, magnons at thermal equilibrium are distributed over energy levels according to Planck's quantum statistics for a given temperature T. This is a Bose-Einstein distribution

with zero chemical potential because the energy and therefore magnon number is not conserved. Nevertheless, it is well established that a magnon chemical potential can parametrize a long-living *nonequilibrium* magnon state. For instance, parametric excitation of a ferromagnet by microwaves generates high-energy magnons that thermalize much faster by magnon-conserving exchange interactions than their number decays [14]. The resulting distribution is very different from a zero-chemical potential quantum or classical distribution function, but is close to an equilibrium distribution with a certain temperature and nonzero chemical potential. The breakdown of even such a description is then indicative of the creation of a Bose (or, in the case of pumping at energies much smaller than the thermal one, Rayleigh-Jeans [15]) condensate. This new state of matter has indeed been observed [16]. Here, we argue that a magnon chemical potential governs spin and heat transport not only under strong parametric pumping, but also in the linear response to weak electric or thermal actuation [17].

The elementary magnetic electron-hole excitations of normal metals or spin accumulation have been a very fruitful concept in spintronics [18]. Since electron thermalization is faster than spin-flip decay, a spin-polarized nonequilibrium state can be described in terms of two Fermi-Dirac distribution functions with different chemical potentials and temperatures for the majority and minority spins. We may distinguish the *spin (particle) accumulation* as the difference between chemical potentials from the *spin heat accumulation* as the difference between the spin temperatures [19]. Both are vectors that are generated by spin injection and governed by diffusion equations with characteristic decay times and lengths. The spin heat accumulation decays faster than the spin particle accumulation since both are dissipated by spin-flip scattering, while the latter is inert to energy exchanging electron-electron interactions. Here, we proceed from the premise that nonequilibrium states of the magnetic order can be described by a Bose-Einstein distribution function for magnons that is parametrized by both temperature and chemical potential,

---

*Corresponding author: l.j.cornelissen@rug.nl

014412-1

where the latter implies magnon number conservation. We therefore define a *magnon heat accumulation* δT_m as the difference between the temperature of the magnons and that of the lattice. The chemical potential μ_m then represents the *magnon spin accumulation*, noting that this definition differs from that by Zhang and Zhang [20], who define a magnon spin accumulation in terms of the magnon density. The crucial parameters are then the relaxation times governing the equilibration of δT_m and μ_m. When the magnon heat accumulation decays faster than the magnon particle accumulation, previous theories for magnonic heat and spin transport should be doubted [1,5–7,21]. The relaxation times are governed by the collision integrals that include inelastic (one-, two-, and three-magnon scatterings involving phonons) and elastic two- and four-magnon scattering processes. At room temperature, two-magnon scattering due to disorder is likely to be negligibly small compared to phonon scattering. Four-magnon scattering only redistributes the magnon energies, but does not lead to momentum or energy loss of the magnon system. Processes that do not conserve the number of magnons are caused by either dipole-dipole or spin-orbit interaction with the lattice and should be less important than the magnon-conserving ones for high-quality magnetic materials such as YIG. At room temperature, the magnon spin accumulation is then essential to describe diffusive spin transport in ferromagnets.

Here, we revisit the linear-response transport theory for magnon spin and heat transport, deriving the spin and heat currents in the bulk of the magnetic insulator as well as across the interface with a normal metal contact. The magnon transport is assumed to be diffusive. Formally we are then limited to the regime in which the thermal magnon wavelength Λ and the magnon mean-free path ℓ (the path length over which magnon momentum is conserved) are smaller than the system size L. The wavelength of magnons in YIG is (in a simple parabolic band model) a few nanometers at room temperature. Boona *et al.* [22] find that ℓ at room temperature is of the same order. As in electron transport in magnetic multilayers, scattering at rough interfaces is likely to render a diffusive picture valid even when the formal conditions for diffusive bulk transport are not met. Under the assumptions that magnons thermalize efficiently and that the mean-free path is dominated by magnon-conserving scattering by phonons or structural and magnetic disorder, we find that the magnon chemical potential is required to harmonize theory and experiments on magnon spin transport [9].

This paper is organized as follows: We start with a brief review of diffusive charge, spin, and heat transport in metals in Sec. II A. In Sec. II B, we derive the linear-response expressions for magnon spin and heat currents, starting from the Boltzmann equation for the magnon distribution function. We proceed with boundary conditions at the Pt|YIG interface in Sec. II C. In Sec. II D, we provide estimates for relaxation lengths and transport coefficients for YIG. The transport equations are analytically solved for a one-dimensional model (longitudinal configuration) in Sec. III A. In Sec. III B, we implement a numerical finite-element model of the experimental geometry and we compare results with experiments in Sec. III C. We apply our model also to the (longitudinal) spin Seebeck effect in Sec. III D. A summary and conclusions are given in Sec. IV.
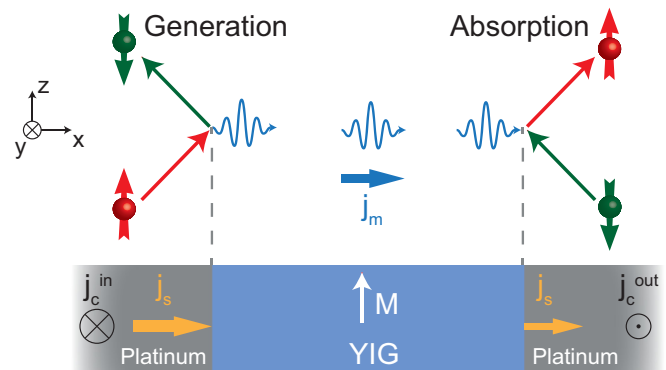

FIG. 1. Schematic of the 1D geometry [13,20]. A charge current j_c^{in} is sent through the left platinum strip along $+\mathbf{y}$. This generates a spin current $j_s = j_{xz} = \theta j_c^{\text{in}}$ towards the YIG|Pt interface and a spin accumulation, injecting magnons into the YIG with spin polarization parallel to the magnetization $\mathbf{M}$. The magnons diffuse towards the right YIG|Pt interface, where they excite a spin accumulation and spin current into the contact. Due to the inverse spin Hall effect, this generates a charge current j_c^{out} along the $-\mathbf{y}$ direction. Note that if $\mathbf{M}$ is aligned along $-\mathbf{z}$, magnons are absorbed at the injector and created at the detector.

II. THEORY

We first review the diffusion theory for electrical magnon spin injection and detection as published by one of us in [17,23]. By introducing the magnon chemical potential, this approach can disentangle spin and heat transport in contrast to earlier treatments based on the magnon density [20] or magnon temperature [1,5–7] only. We initially focus on the one-dimensional (1D) geometry in Fig. 1 with two normal metal (Pt) contacts to the magnetic insulator YIG. We express the spin currents in the bulk of the normal metal contacts and magnetic spacer, and the interface. While Ref. [17] focused on the chemical potential, here we include the magnon temperature as well. At low temperatures, the phonon specific heat has been reported to be an order of magnitude larger than the magnon one [22]. The room-temperature phonon mean-free path (that provides an upper bound for the phonon collision time) of a few nm [22] corresponds to a subpicosecond transport relaxation time for sound velocities of 10^3–10^4 m/s. From the outset, we therefore take the phonon heat capacity to be so large and the phonon mean-free path and collision times so short that the phonon distribution is not significantly affected by the magnons. The phonon temperature T_p is assumed to be either a fixed constant or, in the spin Seebeck case, to have a constant gradient. For simplicity, we also disregard the finite thermal (Kapitza) interface heat resistance of the phonons [24].

A. Spin and heat transport in normal metals

There is much evidence that spin transport in metals is well described by a spin diffusion approximation. Spin-flip diffusion lengths of the order of nanometers reported in platinum betray the existence of large interface contributions [25], but the parametrized theory describes transport well [26]. The charge ($j_{c,\alpha}$), spin ($j_{\alpha\beta}$), and heat ($j_{Q,\alpha}$) current densities in

the normal metals, where the spin polarization is defined in the coordinate system of Fig. 1, are given by (see e.g. [27])

$$j_{c,\alpha} = \sigma_e \partial_\alpha \mu_e - \sigma_e S \partial_\alpha T_e - \frac{\sigma_{\text{SH}}}{2}\epsilon_{\alpha\beta\gamma}\partial_\beta\mu_\gamma,$$

$$\frac{2e}{\hbar}j_{\alpha\beta} = -\frac{\sigma_e}{2}\partial_\alpha\mu_\beta - \sigma_{\text{SH}}\epsilon_{\alpha\beta\gamma}\partial_\gamma\mu_e - \sigma_{\text{SH}}S_{\text{SN}}\epsilon_{\alpha\beta\gamma}\partial_\gamma T_e,$$

$$j_{Q,\alpha} = -\kappa_e\partial_\alpha T_e - \sigma_e P\partial_\alpha\mu_e - \frac{\sigma_{\text{SH}}}{2}P_{\text{SN}}\epsilon_{\alpha\beta\gamma}\partial_\beta\mu_\gamma. \quad (1)$$

Here, μ_e, T_e, and μ_α denote the electrochemical potential, electron temperature, and spin accumulation, respectively. The subscripts $\alpha,\beta,\gamma \in \{x,y,z\}$ are Cartesian components in the coordinate system in Fig. 1, α indicating current direction and β spin polarization. $\epsilon_{\alpha\beta\gamma}$ is the Levi-Civita tensor and the summation convention is assumed throughout. The charge, spin, and heat current densities are measured in units of A/m^2, J/m^2, and W/m^2, respectively, while both the electrochemical potential and the spin accumulation are in volts. The charge and spin Hall conductivities are σ_e and σ_{SH}, both in units of S/m. Thermoelectric effects in metals are governed by the Seebeck coefficient S and Peltier coefficient $P = ST_e$. Similarly, we allow for a spin Nernst effect via the coefficient S_{SN} and the reciprocal spin Ettingshausen effect governed by $P_{\text{SN}} = S_{\text{SN}}T_e$. We assume, however, that spin-orbit coupling is weak enough so that we can ignore spin swapping terms, i.e., terms of the form $j_{\alpha\beta} \sim \partial_\beta\mu_\alpha$ and their Onsager reciprocal [28]. The spin heat accumulation in the normal metal and therefore spin polarization of the heat current are disregarded for simplicity [19]. $\hbar$ and $-e$ are Planck's constant and the electron charge. The continuity equation $\partial_t\rho_e + \nabla \cdot \mathbf{j}_e = 0$ expresses conservation of the electric charge density ρ_e. The electron spin $\boldsymbol{\mu}$ and heat Q_e accumulations relax to the lattice at rates $\Gamma_{s\mu}$ and Γ_{QT}, respectively:

$$\partial_t s_\beta + \frac{1}{\hbar}\partial_\alpha j_{\alpha\beta} = -2\Gamma_{s\mu}e\mu_\beta\nu, \quad (2)$$

$$\partial_t Q_e + \nabla \cdot j_Q = -\Gamma_{QT}C_e(T_e - T_p), \quad (3)$$

where the nonequilibrium spin density $s_\beta = 2e\mu_\beta\nu$, C_e is the electron heat capacity per unit volume, and ν the density of states at the Fermi level. Inserting Eq. (1) leads to the length scales $\ell_s = \sqrt{\sigma_e/(4e^2\Gamma_{s\mu}\nu)}$ and $\ell_{ep} = \sqrt{\kappa_e/(\Gamma_{QT}C_e)}$ governing the decay of the electron spin and heat accumulations, respectively. At room temperature, these are typically $\ell_s^{\text{Pt}} = 1.5$ nm, $\ell_{ep}^{\text{Pt}} = 4.5$ nm for platinum [21,29], and $\ell_s^{\text{Au}} = 35$ nm, $\ell_{ep}^{\text{Au}} = 80$ nm for gold [21,30].

B. Spin and heat transport in magnetic insulators

Magnonics traditionally focuses on the low-energy, long-wavelength regime of coherent wave dynamics. In contrast, the basic and yet not-well-tested assumption underlying the present theory is diffusive magnon transport, which we believe to be appropriate for elevated temperatures in which short-wavelength magnons dominate. Diffusion should be prevalent when the system size is larger than the magnon mean-free path and magnon thermal wavelength (called magnon coherence length in [5]). Magnons carry angular momentum parallel to the magnetization (z axis). Oscillating transverse components of the angular momentum can be safely neglected for system sizes larger than the magnetic exchange length, which is on the order of 10 nm in YIG at low external magnetic fields [8].

Not much is known about the scattering mean-free path, but extrapolating the results from Ref. [22] to room temperature leads to an estimate of a few nm. Dipolar interactions affect mainly the long-wavelength coherent magnons that do not contribute significantly at room temperature. Thermal magnons interact by strong and number-conserving exchange interactions. In the Appendix, the magnon-magnon scattering rate is estimated as $(T/T_c)^3 k_B T/\hbar$ [31,32] or a scattering time of 0.1 ps for YIG with Curie temperature $T_c \sim 500$ K at room temperature $T = 300$ K, where $T \approx T_m \approx T_p$. According to the Landau-Lifshitz-Gilbert phenomenology [33], the magnon decay rate is $\alpha_G k_B T/\hbar$ [32], with Gilbert damping constant $\alpha_G \approx 10^{-4} \ll 1$ for YIG. Hence, the ratio between the scattering rates for magnon-nonconserving to -conserving processes is $\alpha_G(T_c/T)^3 \ll 1$ at room temperature. These numbers justify the second crucial premise of the present formalism, viz., very efficient, local equilibration of the magnon system. Since a spin accumulation in general injects angular momentum and heat at different rates, we need at least two parameters for the magnon distribution f, i.e., an effective temperature T_m and a nonzero chemical potential (or magnon spin accumulation) μ_m in the Bose-Einstein distribution function n_B:

$$f(\mathbf{x},\epsilon) = n_B(\mathbf{x},\epsilon) = \left(e^{\frac{\epsilon-\mu_m(\mathbf{x})}{k_B T_m(\mathbf{x})}} - 1\right)^{-1}, \quad (4)$$

where k_B is Boltzmann's constant. Both magnon accumulations $T_m - T_p$ and μ_m vanish on, in principle, different length scales during diffusion. Assuming an isotropic (cubic) medium, the magnon spin current ($\mathbf{j}_m$, in J/m^2) and heat current densities ($\mathbf{j}_{Q,m}$, in W/m^2) in linear response read as

$$\begin{pmatrix} \frac{2e}{\hbar}\mathbf{j}_m \\ \mathbf{j}_{Q,m} \end{pmatrix} = -\begin{pmatrix} \sigma_m & L/T \\ \hbar L/2e & \kappa_m \end{pmatrix}\begin{pmatrix} \boldsymbol{\nabla}\mu_m \\ \boldsymbol{\nabla}T_m \end{pmatrix}, \quad (5)$$

where μ_m is measured in volts, σ_m is the magnon spin conductivity (in units of S/m), L is the (bulk) spin Seebeck coefficient in units of A/m, and κ_m is the magnonic heat conductivity in units of Wm^{-1}K^{-1}. Magnon-phonon drag contributions $\mathbf{j}_m, \mathbf{j}_{Q,m} \propto \boldsymbol{\nabla}T_p$ are assumed to be absorbed in the transport coefficients since $T_m \approx T_p$. The spin and heat continuity equations for magnon transport read as

$$\begin{pmatrix} \frac{\partial\rho_m}{\partial t} + \frac{1}{\hbar}\boldsymbol{\nabla}\cdot\mathbf{j}_m \\ \frac{\partial Q_m}{\partial t} + \boldsymbol{\nabla}\cdot\mathbf{j}_{Q,m} \end{pmatrix} = -\begin{pmatrix} \Gamma_{\rho\mu} & \Gamma_{\rho T} \\ \Gamma_{Q\mu} & \Gamma_{QT} \end{pmatrix}\begin{pmatrix} \mu_m\frac{\partial\rho_m}{\partial\mu_m} \\ C_m(T_m - T_p) \end{pmatrix}, \quad (6)$$

in which ρ_m is the nonequilibrium magnon spin density and Q_m the magnonic heat accumulation. C_m is the magnon heat capacity per unit volume. The rates $\Gamma_{\rho\mu}$ and Γ_{QT} describe relaxation of magnon spin and temperature, respectively. The cross terms (decay or generation of spins by cooling or heating of the magnons and vice versa) are governed by the coefficients $\Gamma_{\rho T}$ and $\Gamma_{Q\mu}$. Equations (5) and (6) lead to the diffusion equations

$$\begin{pmatrix} e & \alpha_\mu k_B \\ e\alpha_T/k_B & 1 \end{pmatrix}\begin{pmatrix} \nabla^2\mu_m \\ \nabla^2 T_m \end{pmatrix}$$

$$= \begin{pmatrix} e/\ell_m^2 & k_B/(\ell_{\rho T}T^2) \\ e/(k_B\ell_{Q\mu}\mu_m^2) & 1/\ell_{\text{mp}}^2 \end{pmatrix}\begin{pmatrix} \mu_m \\ T_m - T_p \end{pmatrix}, \quad (7)$$
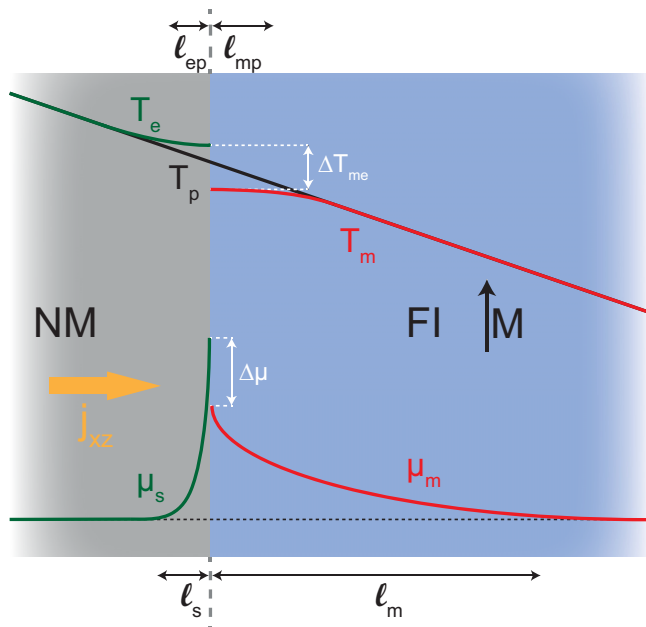
FIG. 2. Length scales at normal metal|ferromagnetic insulator (NM|FI) interfaces in Fig. 1. Assuming a constant gradient of the phonon temperature T_p and disregarding Joule heating, the electron temperature T_e and magnon temperature T_m relax on length scales ℓ_{ep} and ℓ_{mp}. A significant phonon heat (Kapitza) resistance would cause a step in T_p at the interface. The spin Hall effect in the normal metal drives a spin current j_{xz} towards the interface, which will be partially transmitted to the magnon system (causing a nonzero magnon chemical potential in the FI) and partially reflected back into the NM (causing a nonzero electron spin accumulation in the NM). The electron spin accumulation $\mu_s = \mu_z$ and the magnon chemical potential μ_m relax on length scales ℓ_s and ℓ_m, respectively.

with four length scales and two dimensionless ratios. Here, $\ell_m = \sqrt{\sigma_m/(2e\Gamma_{\rho\mu})(\frac{\partial\rho_m}{\partial\mu_m})^{-1}}$ is the magnon spin diffusion length (or relaxation length of the magnon chemical potential) and $\ell_{mp} = \sqrt{\kappa_m/(\Gamma_{QT}C_m)}$ is the magnon-phonon relaxation length that governs the relaxation of the magnon temperature. The equilibrium values for magnon chemical potential and magnon temperature are $\mu_m = 0$ and $T_m = T_p$ (see Fig. 2). The length scales $\ell_{\rho T} = \sqrt{k_B\sigma_m/(2e^2\Gamma_{\rho T}C_m)}$ and $\ell_{Q\mu} = \sqrt{e\kappa_m/(\hbar k_B\Gamma_{Q\mu})(\frac{\partial\rho_m}{\partial\mu_m})^{-1}}$ arise from the nondiagonal cross terms. The dimensionless ratio $\alpha_\mu = eL/(k_B\sigma_m T_p)$ is a measure for the relative ability of chemical-potential and temperature gradients to drive spin currents. Similarly, $\alpha_T = \hbar k_B L/(2e\kappa_m)$ characterizes the magnon heat current driven by chemical potential gradients relative to that driven by temperature gradients.

C. Interfacial spin and heat currents

The electron and magnon diffusion equations are linked by interface boundary conditions. Spin currents and accumulations are parallel to the magnetization direction of the ferromagnet along the z direction. We assume that the exchange coupling dominates the coupling between electrons and magnons across the interface. A perturbative treatment of the exchange coupling at the interface leads to the spin

current [34,35]

$$j_s^{\text{int}} = -\frac{\hbar\, g^{\uparrow\downarrow}}{2e^2\pi s}\int d\epsilon\, D(\epsilon)(\epsilon - e\mu_z)$$
$$\times\left[n_B\left(\frac{\epsilon - e\mu_m}{k_B T_m}\right) - n_B\left(\frac{\epsilon - e\mu_z}{k_B T_e}\right)\right], \quad (8)$$

where $g^{\uparrow\downarrow}$ is the real part of the spin-mixing conductance in S/m^2, $s = S/a^3$ the equilibrium spin density of the magnetic insulator, and S is the total spin in a unit cell with volume a^3. The density of states of magnons $D(\epsilon) = \sqrt{\epsilon - \Delta}/(4\pi^2 J_s^{3/2})$ for a dispersion $\hbar\omega_\mathbf{k} = J_s\mathbf{k}^2 + \Delta$. The spin-wave gap Δ is governed by the magnetic anisotropy and the applied magnetic field. In soft ferromagnets such as YIG $\Delta \sim 1$ K, which we disregard in the following since we focus on effects at room temperature (see e.g. Ref. [8]). The heat current is given by inserting $\epsilon/\hbar$ into the integrand of Eq. (8).

Linearizing the above equation, we find the spin and heat currents across the interface [17]

$$\begin{pmatrix} j_s^{\text{int}} \\ j_Q^{\text{int}} \end{pmatrix} = \frac{3\hbar\, g^{\uparrow\downarrow}}{4e^2\pi s\Lambda^3}\begin{pmatrix} e\,\zeta(3/2) & \frac{5}{2}k_B\zeta(5/2) \\ \frac{5}{2}\frac{ek_B T}{\hbar}\zeta(5/2) & \frac{35}{4}\frac{k_B^2 T}{\hbar}\zeta(7/2) \end{pmatrix}$$
$$\times\begin{pmatrix} \mu_z - \mu_m \\ T_e - T_m \end{pmatrix}. \quad (9)$$

$\Lambda = \sqrt{4\pi J_s/(k_B T)}$ is the magnon thermal (de Broglie) wavelength (the factor 4π is included for convenience). These expressions agree with those derived from a stochastic model [5] after correcting numerical factors of the order of unity. In YIG at room temperature $\Lambda \sim 1$ nm. The term proportional to μ_z corresponds to the spin transfer (absorption of spin current by the fluctuating magnet), while that proportional to μ_m is the spin pumping contribution (emission of spin current by the magnet). The prefactor $\sim 1/(s\Lambda^3)$ can be understood by noting that $s\Lambda^3$ is the effective number of spins in the magnetic insulator that has to be agitated and appears in the denominator of Eq. (9) as a mass term. In the macrospin approximation, this term would be replaced by the total number of spins in the magnet.

From Eq. (9) we identify the effective spin conductance g_s that governs the transfer of spin across the interface by the chemical potential difference $\Delta\mu = \mu_z - \mu_m$. In units of S/m^2,

$$g_s = \frac{3\,\zeta\left(\frac{3}{2}\right)}{2\pi s}\frac{g^{\uparrow\downarrow}}{\Lambda^3}. \quad (10)$$

Using the material parameters for YIG from Table II and the expression for the thermal de Broglie wavelength given above, we find $g_s = 0.06g^{\uparrow\downarrow}$ at room temperature [21,36]. g_s scales with temperature like $\sim(T/T_c)^{3/2}$, but it should be kept in mind that the theory is not valid in the limits $T \to T_c$ and $T \to 0$. It is nevertheless consistent with the recently reported strong suppression of g_s at low temperatures [10,13].

D. Parameters and length scales

In this section, we present expressions for the transport parameters derived from the linearized Boltzmann equation for the magnon distribution function and present numerical estimates based on experimental data.

TABLE I. Transport coefficients and length scales [17] as derived in the Appendix.

	Symbol	Expression
Magnon thermal de Broglie wavelength	Λ	$\sqrt{4\pi J_s/(k_B T)}$
Magnon spin conductivity	σ_m	$4\zeta(3/2)^2 e^2 J_s \tau/(\hbar^2 \Lambda^3)$
Magnon heat conductivity	κ_m	$\frac{35}{2}\zeta(7/2) J_s k_B^2 T \tau/(\hbar^2 \Lambda^3)$
Bulk spin Seebeck coefficient	L	$10\zeta(5/2) e J_s k_B T \tau/(\hbar^2 \Lambda^3)$
Magnon thermal velocity	$v_{\rm th}$	$2\sqrt{J_s k_B T}/\hbar$
Magnon spin diffusion length	ℓ_m	$v_{\rm th}\sqrt{\frac{2}{3}\tau\tau_{\rm mr}}$
Magnon-phonon relaxation length	$\ell_{\rm mp}$	$v_{\rm th}\sqrt{\frac{2}{3}\tau(1/\tau_{\rm mr} + 1/\tau_{\rm mp})^{-1}}$
Magnon spin-heat relaxation length	$\ell_{\rho T}$	$\ell_m/\sqrt{\alpha_\mu}$
Magnon heat-spin relaxation length	$\ell_{Q\mu}$	$\ell_m/\sqrt{\alpha_T}$
	α_μ	$\frac{5}{2}\zeta(5/2)/\zeta(3/2)$
	α_T	$\frac{2}{7}\zeta(5/7)/\zeta(7/2)$

1. Boltzmann transport theory

Magnon transport as formulated in the previous section is governed by the transport coefficients σ_m, L, κ_m, four length scales ℓ_m, $\ell_{\rm mp}$, $\ell_{\rho T}$, and $\ell_{Q\mu}$, and two dimensionless numbers α_μ and α_T. In the Appendix, we derive these parameters using the linearized Boltzmann equation in the relaxation time approximation. We consider four interaction events: (i) elastic magnon scattering by bulk impurities or interface disorder, (ii) magnon dissipation by magnon-phonon interactions that annihilate or create spin waves and/or inelastic scattering of magnons by magnetic disorder, (iii) magnon-phonon interactions that conserve the number of magnons, and (iv) magnon-magnon scattering by magnon-conserving exchange scattering processes (see also Sec. II B).

The magnon energy and momentum-dependent scattering times for these processes are $\tau_{\rm el}$, $\tau_{\rm mr}$, $\tau_{\rm mp}$, and $\tau_{\rm mm}$. At elevated temperatures they should be computed at magnon energy $k_B T$ and momentum $\hbar/\Lambda$. Magnon-magnon interactions that conserve momentum do not directly affect transport currents in our single magnon band model, so the total relaxation rate is $1/\tau = 1/\tau_{\rm el} + 1/\tau_{\rm mr} + 1/\tau_{\rm mp}$.

The transport coefficients and length scales derived in the Appendix are summarized in Table I. The Einstein relation $\sigma_m = 2e D_m \partial\rho_m/\hbar\partial\mu_m$ connects the magnon diffusion constant D_m defined by $\mathbf{j}_m = -D_m \nabla \rho_m$ with the magnon conductivity, where $\partial\rho_m/\partial\mu_m = e\mathrm{Li}_{1/2}(e^{-\Delta/k_B T})/(4\pi\Lambda J_s)$ and $\mathrm{Li}_n(z)$ is the polylogarithmic function of order n.

We observe that the magnon-phonon relaxation length $\ell_{\rm mp}$ is smaller than the magnon spin diffusion length ℓ_m since the latter is proportional to $\tau_{\rm mr}$, whereas $\ell_{\rm mp}$ is limited by both magnon-conserving and -nonconserving scattering processes. Furthermore, $1/\tau_{\rm mr}$ can be estimated by the Landau-Lifshitz-Gilbert equation as $\sim\alpha_G k_B T/\hbar$ [32], where the Gilbert constant α_G at thermal energies is not necessarily the same as for ferromagnetic resonance.

2. Clean systems

In the limit of a clean system, $1/\tau_{\rm el} \to 0$. At sufficiently low temperatures, the magnon-conserving magnon-phonon scattering rate $1/\tau_{\rm mp} \sim T^{3.5}$ [37] (see also the Appendix)

loses against $1/\tau_{\rm mr} \sim \alpha_G k_B T/\hbar$ since α_G is approximately temperature independent. Then, all lengths $\sim\Lambda/\alpha_G \sim 10\ \mu$m for YIG at room temperature and with $\alpha_G = 10^{-4}$ from ferromagnetic resonance (FMR) [8]. The agreement with the observed signal decay [9] is likely to be coincidental, however, since the spin waves at thermal energies have a much shorter lifetime than the Kittel mode for which α_G is measured. σ_m estimated using the FMR Gilbert damping is larger than the experimental value by several orders of magnitude, which is a strong indication that the clean limit is not appropriate for realistic devices at room temperature.

3. Estimates for YIG at room temperature

The phonon and magnon inelastic mean-free paths derived from the experimental heat conductivity appear to be almost identical at low temperatures up to 20 K [22] but could not be measured at higher temperatures. Both are likely to be limited by the same scattering mechanism, i.e., the magnon-phonon interaction. We assume here that the magnon-phonon scattering of thermal magnons at room temperature is dominated by the exchange interaction (which always conserves magnons) rather than the magnetic anisotropy (which may not conserve magnons) [38]. Then, $\tau \sim \tau_{\rm mp}$ and extrapolating the low-temperature results to room temperature leads to an $\ell_{\rm mp}$ of the order of a nm, in agreement with an analysis of spin Seebeck [6] and Peltier [21] experiments. The associated time scale $\tau_{\rm mp} \sim 1$–0.1 ps is of the same order as $\tau_{\rm mm}$ estimated in Sec. II B. On the other hand, $\tau_{\rm mr} \sim 1$ ns from $\alpha_G \sim 10^{-4}$ and therefore $\ell_m \sim v_{\rm th}\sqrt{\tau_{\rm mp}\tau_{\rm mr}} \sim 0.1$–$1\ \mu$m. The observed magnon spin transport signal decays over a somewhat longer length scale ($\sim 10\ \mu$m). Considering that the estimated $\tau_{\rm mr}$ is an upper limit, our crude model apparently overestimates the scattering. An important conclusion is, nonetheless, that $\ell_m \gg \ell_{\rm mp}$, which implies that the magnon chemical potential carries much farther than the magnon temperature.

With $\tau \sim \tau_{\rm mp} \sim 0.1$–1 ps we can also estimate the magnon spin conductivity $\sigma \sim e^2 J_s \tau/\hbar^2 \Lambda^3 \sim 10^5$–$10^6$ S/m, in reasonable agreement with the value extracted from our experiments (see next section).

III. HETEROSTRUCTURES

Here, we apply the model, introduced and parametrized in the previous section, to concrete contact geometries and compare the results with experiments. We start with an analytical treatment of the one-dimensional geometry, followed by numerical results for the transverse configuration of top metal contacts on a YIG film with finite thickness. Throughout, we assume, motivated by the estimates presented in the previous section, that the magnon-phonon relaxation is so efficient that the magnon temperature closely follows the phonon temperature, i.e., $T_m = T_p$ (only in Sec. III C 3 we study the implications of the opposite case, i.e., $T_m \neq T_p$ and $\mu_m = 0$). This allows us to focus on the spin diffusion equation for the chemical potential μ_m. This approximation should hold at room temperature, while the opposite regime $\ell_{mp} \gg \ell_m$ might be relevant at low temperatures or high magnon densities: when the magnon chemical potential is pinned to the band edge, transport can be described in terms of the effective magnon temperature. The intermediate regime $\ell_{mp} \sim \ell_m$, in which both magnon chemical potential and effective temperature have to be taken into account, is left for future study.

A. One-dimensional model

We consider first the one-dimensional geometry shown in Fig. 1. We focus on strictly linear response and therefore disregard Joule heating in the metal contacts as well as thermoelectric voltages by the spin Nernst and Ettingshausen effects. The spin and charge currents in the metal are then governed by

$$\begin{pmatrix} j_c \\ \frac{2e}{\hbar} j_s \end{pmatrix} = \begin{pmatrix} \sigma_e & -\sigma_{\mathrm{SH}} \\ -\sigma_{\mathrm{SH}} & -\sigma_e \end{pmatrix} \begin{pmatrix} \partial_y \mu_e \\ \frac{1}{2} \partial_x \mu_z \end{pmatrix}, \qquad (11)$$

where the charge transport is in the y direction, spin transport in the x direction, and the electron spin accumulation is pointing in the z direction. The spin and magnon diffusion equations reduce to

$$\frac{\partial^2 \mu_s}{\partial x^2} = \frac{\mu_z}{\ell_s^2}, \qquad (12)$$

$$\frac{\partial^2 \mu_m}{\partial x^2} = \frac{\mu_m}{\ell_m^2}. \qquad (13)$$

The interface spin currents (8) provide the boundary conditions at the interface to the ferromagnet, while all currents at the vacuum interface vanish. Equations (9) and (10) lead to the interface spin current density $j_s^{\mathrm{int}} = g_s(\mu_z^{\mathrm{int}} - \mu_m^{\mathrm{int}})$, where g_s is defined in Eq. (10).

1. Current transfer efficiency

The nonlocal resistance R_{nl} is the voltage over the detector divided by current in the injector, also referred to as nonlocal spin Hall magnetoresistance (see below). The magnon spin injection and detection can also be expressed in terms of the current transfer efficiency η, i.e., the absolute value of the ratio between the currents in the detector and injector strip [20] when the detector circuit is shorted. $\eta = R_{\mathrm{nl}}/R_0$ for identical Pt contacts with resistance R_0. In Fig. 3, we
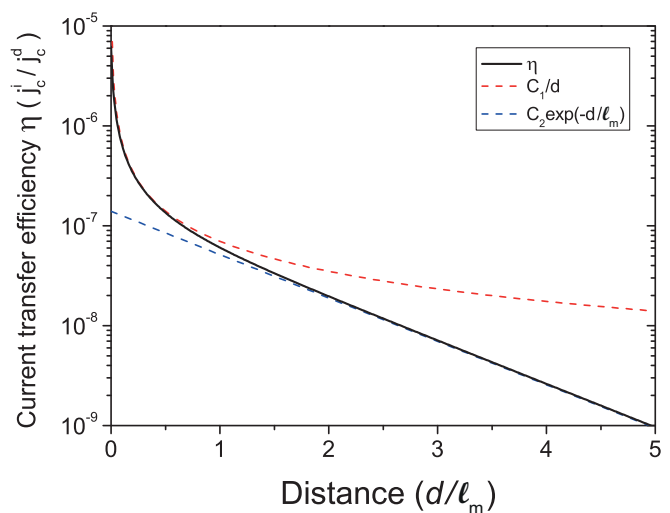

FIG. 3. The current transfer efficiency η (nonlocal resistance normalized by that of the metal contacts) as a function of distance between the contacts in a Pt|YIG|Pt structure calculated in the 1D model. Parameters are taken from Table II and the Pt thickness $t = 10$ nm. The dashed lines are plots of the functions C_1/d (red dashed line) and $C_2 \exp(-d/\ell_m)$ (blue dashed line) to show the different modes of signal decay in different regimes: diffusive $1/d$ decay for $d < \ell_m$ and exponential decay for $d > \ell_m$. The constants C_1 and C_2 were chosen to show overlap with η for illustrative purposes, but have no physical meaning.

plot the calculated η as a function of distance d between the contacts for a Pt thickness $t = 10$ nm and parameters from Table II. η decays algebraically $\propto 1/d$ when $d \ll \ell_m$, which implies diffusion without relaxation, and exponentially for $d \gg \ell_m$. The calculated order of magnitude already agrees with experiments [9]. The η's in Ref. [20] are three orders of magnitude larger than ours due to their much weaker relaxation.

TABLE II. Selected parameters for spin and heat transport in bilayers with magnetic insulators and metals. a, S, and J_s are adopted from [39], ℓ_s and θ from [21,29], and σ_e is extracted from electrical measurements on our devices [9]. Note that our values for σ_e and ℓ_s are consistent with Elliot-Yafet scattering as the dominant spin relaxation mechanism in platinum [40]. The mixing conductance, magnon spin diffusion length, and the magnon spin conductivity are estimated in the main text.

|	Symbol	Value	Unit
YIG lattice constant	a	12.376	Å
Spin quantum number per YIG unit cell	S	10	
Spin-wave stiffness constant in YIG	J_s	8.458×10^{-40}	Jm^2
YIG magnon spin diffusion length	ℓ_m	9.4	μm
YIG spin conductivity	σ_m	5×10^5	S/m
Real part of the spin-mixing conductance	$g^{\uparrow\downarrow}$	1.6×10^{14}	S/m^2
Platinum conductivity	σ_e	2.0×10^6	S/m
Platinum spin relaxation length	ℓ_s	1.5	nm
Platinum spin Hall angle	θ	0.11	
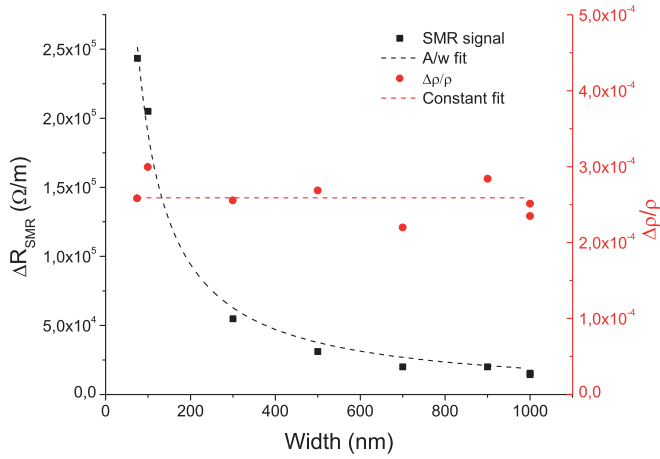
FIG. 4. Experimental spin Hall magnetoresistance (SMR) as a function of platinum strip width. The black squares (left axis) show absolute resistance changes ΔR_{SMR} divided by the device length (18 μm) in units of Ω/m. The red dots (right axis) show the relative resistivity changes $\Delta\rho/\rho$.

The origin of the small η is the inefficiency of the spin Hall mediated spin-charge conversion. The ratio between the spin accumulations in injector and detector $\eta_s = \mu_s^{\text{det}}/\mu_s^{\text{inj}}$ is much larger than η and discussed in Sec. III C 2.

2. Spin Hall magnetoresistance

The effective spin conductance g_s governs the amount of spin transferred across the interface between the normal metal and the magnetic insulator. While g_s cannot be extracted from measurements directly, it is related to the spin-mixing conductance $g^{\uparrow\downarrow}$ via Eq. (10). In order to determine $g^{\uparrow\downarrow}$ we measured the spin Hall magnetoresistance (SMR) [41,42] in devices of Ref. [9]. The SMR is defined as the relative resistivity change in the Pt contact between in-plane magnetization parallel and normal to the current $\Delta\rho/\rho$. The expression for the magnitude of the SMR reads as [43]

$$\frac{\Delta\rho}{\rho} = \theta^2 \frac{\ell_s}{t} \frac{2\ell_s g^{\uparrow\downarrow} \tanh^2 \frac{t}{2\ell_s}}{\sigma_e + 2\ell_s g^{\uparrow\downarrow} \coth \frac{t}{\ell_s}}, \quad (14)$$

where $t = 13.5$ nm is the platinum thickness. Figure 4 shows the experimental SMR as a function of platinum strip width. As expected $\Delta\rho/\rho = (2.6 \pm 0.09) \times 10^{-4}$ does not depend on the strip width. Using Eq. (14) and the values for ℓ_s, θ, and σ_e as indicated in Table II, we find $g^{\uparrow\downarrow} = (1.6 \pm 0.06) \times 10^{14}$ S/m^2, which agrees with previous reports [29,42,44].

In Chen *et al.*'s zero-temperature theory [43] the spin current generated by the spin Hall effect in Pt is perfectly reflected when spin accumulation and magnetization are collinear. As discussed above, at finite temperature a fraction of the spin current is injected into the ferromagnet in the form of magnons. This implies that the SMR should be a monotonously decreasing function of temperature. This has been found for high temperatures [45], but the decrease of the SMR at low temperatures [46] hints at a temperature dependence of other parameters such as the spin Hall angle.

The current transfer efficiency η can be interpreted as a nonlocal version of the SMR [10]. The SMR is caused by

the contrast in spin current absorption of the YIG|Pt interface when the spin accumulation vector is normal or parallel to the magnetization **M**. In the nonlocal geometry, we measure the voltage in contact 2 that has been induced by a charge current (in the same direction) in contact 1. Since $g_s < g^{\uparrow\downarrow}$, the relation $|\Delta\rho/\rho| \geqslant \eta$ must hold even in the absence of losses in the ferromagnet and detector. This indeed agrees with our data.

3. Interface transparency

The analytical expression for η in the one-dimensional geometry is lengthy and omitted here, but it can be simplified for special cases. In the limit of a large bulk magnon spin resistance, the interface resistance can be disregarded. The decay of the spin current is then dominated by the bulk spin resistance and relaxation of both materials. When $\sigma_m/\ell_m, \sigma_e/\ell_s \ll g_s$

$$\eta = \frac{\theta^2 \ell_m \sigma_e \sigma_m}{t\left[\sigma_m^2 + \left(\frac{\ell_m}{\ell_s}\right)^2 \sigma_e^2\right]} \sinh^{-1} \frac{d}{\ell_m}, \quad (15)$$

where the Pt thickness is chosen $t \gg \ell_s$ and $\theta = \sigma_{\text{SH}}/\sigma_e$ is the spin Hall angle. When $d \ll \ell_m$ we are in the purely diffusive regime with algebraic decay $\eta \propto 1/d$. Exponential decay with characteristic length ℓ_m takes over when $d \gtrsim \ell_m$. In our experiments (see Table II) $\sigma_m \sim \sigma_e$ and $\ell_m \gg \ell_s$, so

$$\eta = \frac{\theta^2 \ell_s^2 \sigma_m}{\ell_m t \sigma_e} \sinh^{-1} \frac{d}{\ell_m}. \quad (16)$$

On the other hand, when $\sigma_m/\ell_m, \sigma_e/\ell_s \gg g_s$ the interfaces dominate and

$$\eta = \frac{\theta^2 g_s^2 \ell_s^2 \ell_m}{t \sigma_e \sigma_m} \sinh^{-1} \frac{d}{\ell_m}, \quad (17)$$

with identical scaling with respect to d, but a different prefactor. According to the parameters in Table II $\sigma_m/\ell_m \gg \sigma_e/\ell_s \gg g_s$, so spin injection is limited by the interfaces due to the small spin conductance between YIG and platinum.

B. Two-dimensional geometry

Experiments are carried out for Pt|YIG|Pt with a lateral (transverse) geometry in which the platinum injector and detector are deposited on a YIG film. The two-dimensional model sketched in Fig. 5 captures this configuration but cannot be treated analytically. We therefore developed a finite-element implementation of our spin diffusion theory by the COMSOL MULTIPHYSICS (version 4.3a) software package, extending the description of spin transport in metallic systems [47] to magnetic insulators. The finite-element simulations of the spin Seebeck [6] and spin Peltier [21] effects in Pt|YIG focused on heat transport and were based on a magnon temperature diffusion model. Here, we find that neglecting the magnon chemical potential underestimates spin transport by orders of magnitude because the magnon temperature equilibrates at a length scale ℓ_{mp} of a few nanometers and the magnon heat capacity and heat conductivity are small [22]. The magnon chemical potential and the associated nonequilibrium magnons, on the other hand, diffuse on the much longer length scale ℓ_m.
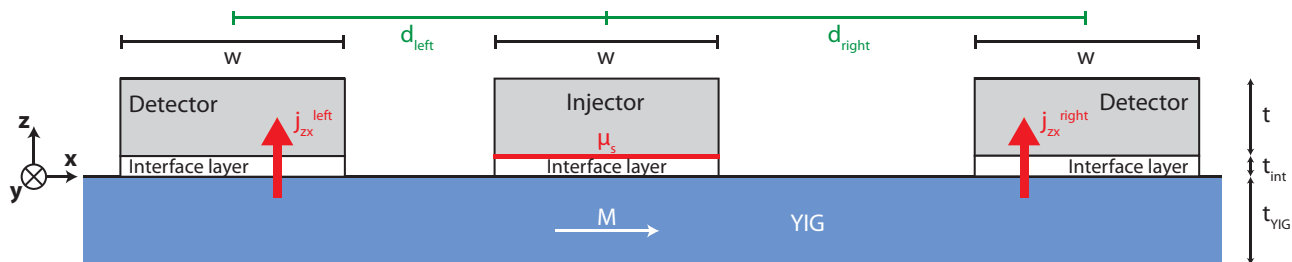
FIG. 5. Schematic of the 2D geometry. The relevant dimensions are indicated in the figure. The spin accumulation arising from the charge current through the injector μ_s is used as a boundary condition on the YIG|Pt interface. The interface layer is used to account for the effect of finite spin-mixing conductance between YIG and platinum.

In order to model the experiments in two dimensions, we assume translational invariance in the third direction, which is justified by the large aspect ratio of relatively small contact distances compared with their length. With equal magnon and phonon temperatures everywhere, the magnon transport in two dimensions is governed by

$$\frac{2e}{\hbar}\mathbf{j}_m = -\sigma_m \nabla \mu_m,$$

$$\nabla^2 \mu_m = \frac{\mu_m}{\ell_m^2}, \tag{18}$$

where $\nabla = \mathbf{x}\partial_x + \mathbf{z}\partial_z$.

The particle spin current $\mathbf{j}_s = (j_{xx}, j_{zx})$ in the metal is described by

$$\frac{2e}{\hbar}\mathbf{j}_s = -\frac{\sigma_e}{2}\nabla \mu_x,$$

$$\nabla^2 \mu_x = \frac{\mu_x}{\ell_s^2}, \tag{19}$$

where μ_x is the x component of the electron spin accumulation. The spin-charge coupling via the spin Hall effect is implemented by the boundary conditions in Sec. III B 2, while the inverse spin Hall effect is accounted for in the calculation of the detector voltage (see Sec. III B 5). The estimates at the end of the previous section justify disregarding temperature effects.

1. Geometry

In order to accurately model the experiments, we define two detectors (left and right) and a central injector, introducing the distances d_{left} and d_{right} as in Fig. 5. We generate a short- (A) and a long-distance (B) geometry. The injector and detectors are slightly different as summarized in Table III. The YIG film thicknesses are 200 nm for (A) and 210 nm for (B). The YIG film is chosen to be long compared to the spin diffusion length ($w_{\text{YIG}} = 150 \ \mu\text{m}$) in order to prevent finite-size artifacts.

TABLE III. Properties of geometry sets A and B.

	Pt width w (nm)	Pt thickness t (nm)	Distances d (μm)
Geometry A	140	13.5	0.2–5
Geometry B	300	7	2–42.5

2. Boundary conditions

Sending a charge current density j_c in the $+y$ direction through the platinum injector strip generates a spin accumulation μ_s at the YIG|platinum interface by the spin Hall effect (shown in Fig. 5). This is captured by Eq. (1) that predicts a spin accumulation at the Pt side of the interface of [21]

$$\mu_s \equiv \mu_{x|\text{interface}} = 2\theta j_c \frac{\ell_s}{\sigma_e} \tanh\left(\frac{t}{2\ell_s}\right), \tag{20}$$

which is used for the interface boundary condition of the magnon diffusion equation. Here, we assume that the contact with the YIG does not significantly affect the spin accumulation [43], which is allowed for the collinear configuration since $g_s < \sigma_e/\ell_s$. The spin orientation of μ_s points along $-\mathbf{x}$, parallel to the YIG magnetization. A charge current $I = 100 \ \mu\text{A}$ generates spin accumulations in the injector contact of $\mu_s^A = 8.7 \ \mu\text{V}$ and $\mu_s^B = 7.7 \ \mu\text{V}$ for geometries A and B, respectively.

The uncovered YIG surface is subject to a zero current boundary condition $(\nabla \cdot \mathbf{n})\mu_s = \mathbf{0}$, where $\mathbf{n}$ is the surface normal.

3. YIG|Pt interface

The interface spin conductance g_s is modeled by a thin interface layer, leading to a spin current $j_s^{\text{int}} = -\sigma_s^{\text{int}}\partial\mu_x/\partial z$, with spin conductivity $\sigma_s^{\text{int}} = g_s t_{\text{int}}$. When the interface thickness t_{int} is small compared to the platinum thickness t_{Pt} we can accurately model the Pt|YIG interface without having to change the COMSOL code. Varying the auxiliary interface layer thickness between $0.5 < t_{\text{int}} < 2.5$ nm, the spin currents change by only 0.1%. This is expected because the increased interface layer thickness is compensated by the reduced resistivity of the interface material such that the resistance remains constant. In the following, we adopt $t_{\text{int}} = 1.0$ nm.

Finally, with Eq. (10) $g_s = 0.06g^{\uparrow\downarrow}$ and $g^{\uparrow\downarrow}$ from Sec. III A 2 we get $g_s = 9.6 \times 10^{12}$ S/m^2.

4. Magnon chemical potential profile

A representative computed magnon chemical potential map is shown in Fig. 6(a), while different profiles along the three indicated cuts are plotted in Figs. 6(b)–6(d). The magnon chemical potential along x and at $z = -1$ nm (i.e., 1 nm below the surface of the YIG) in Fig. 6(b) is characterized by the spin injection by the center electrode. Globally, μ_m decays exponentially with distance from the injector on the scale of ℓ_m.
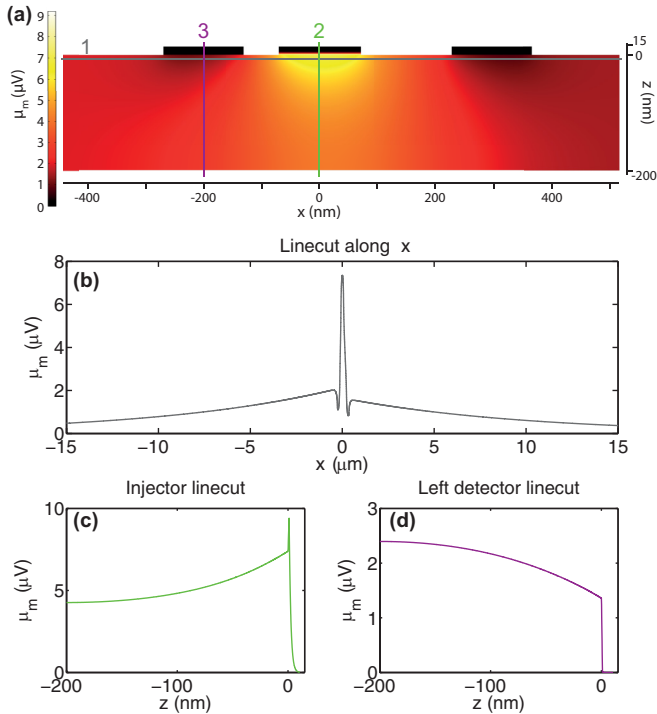
FIG. 6. (a) Two-dimensional magnon chemical potential distribution for geometry (A) with $d_{\text{left}} = 200$ nm and $d_{\text{right}} = 300$ nm. The lines numbered 1, 2, 3 indicate the locations of the profiles plotted in figures (b), (c), (d), respectively. In (b) we observe a maximum μ_m for $x = 0$, i.e., under the injector, followed by a sharp decrease close to the detectors located at $x = -200$ and 300 nm because the Pt contacts are efficient (but not ideal) spin sinks. On the outer sides of the detectors μ_m partially recovers with distance and finally decays exponentially on the length scale ℓ_m.

We also observe that the left and right detector contacts at $x = -200$ nm and 300 nm, respectively, act as sinks that visibly suppress but do not quench the magnon accumulation. The finite mixing conductance and therefore magnon absorption are also evident from the profiles along z in Figs. 6(c) and 6(d):
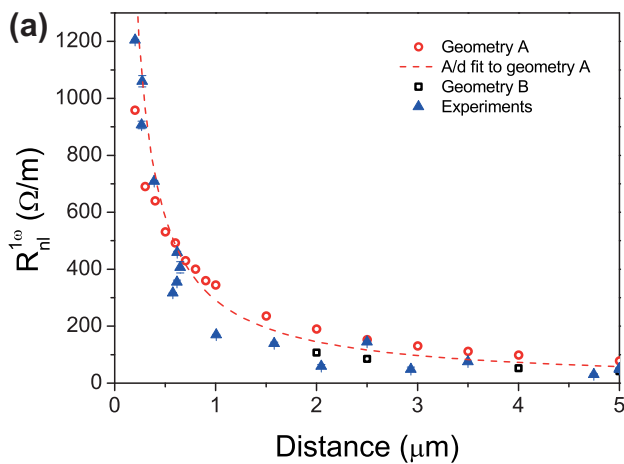
the magnon chemical potential changes abruptly across the YIG|Pt interface by the relatively large interface resistance g_s^{-1}. The magnon chemical potential is much smaller than the magnon gap (~ 1 K). We are therefore far from the threshold for current-driven instabilities such as magnon condensation and/or self-oscillations of the magnetization [32].

5. Detector contact and nonlocal resistance

The spin current density in the detectors is governed by the spin accumulation according to

$$\langle j_{zx} \rangle = -\frac{\sigma_e}{2A} \int_A \frac{\partial \mu_x}{\partial z} dA', \tag{21}$$

which is an average over the detector area $A = wt$. The observable nonlocal resistance R_{nl} (normalized to device length) in units of Ω/m,

$$R_{\text{nl}} = \frac{\theta \langle j_{zx} \rangle}{\sigma_e I}, \tag{22}$$

is compared with experiments in the next section.

C. Comparison with experiments

1. Two-dimensional model

Figure 7 compares the simulations as described in the previous section with our experiments [9]. Figure 7(a) is a linear plot for closely spaced Pt contacts while Fig. 7(b) shows the results for all contact distances on a logarithmic scale. The magnon spin conductivity σ_m and the magnon spin diffusion length ℓ_m are adjustable parameters; all others are listed in Table II. We adopted $\sigma_m = 5 \times 10^5$ S/m and $\ell_m = 9.4$ μm as the best fit values that agree with the estimates in Ref. [9] and Sec. II D.

At large contact separations in geometry (B), the signal is more sensitive to the bulk parameters ℓ_m and σ_m than the interface g_s. When contacts are close to each other, the interfaces become more important and the results depend sensitively on g_s and σ_m as compared to ℓ_m. For very close contacts ($d < 500$ nm) the total spin resistance of YIG is dominated by the interface and our model calculations slightly
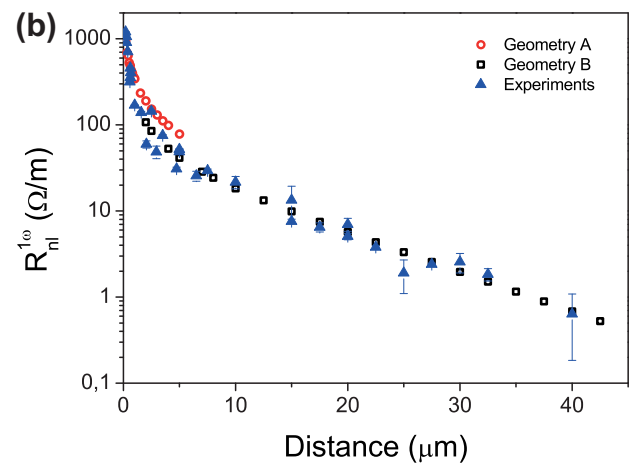

FIG. 7. (a) Computed nonlocal first harmonic signal as a function of distance on a linear scale. The red open circles show the results for sample (A), while black open squares represent sample (B). The blue triangles are the experimental results [9]. The red dashed line is a $1/d$ fit of the numerical results for (A). (b) Same as (a) but on a logarithmic scale.
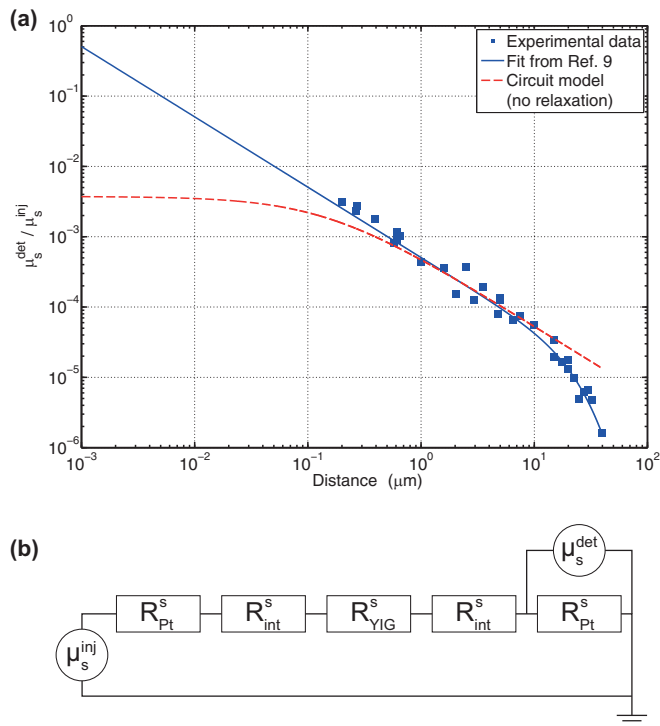
(a)

(b)

FIG. 8. (a) Experimental and simulated spin transfer efficiency $\eta_s = \mu_s^{det}/\mu_s^{inj}$. The blue solid line is a fit by the 1D spin diffusion model [9]. Since here interfaces are disregarded, $\mu_s^{det} \rightarrow \mu_s^{inj}$ for vanishing contact distances. The red dashed line is obtained from the equivalent circuit model in (b) with spin resistances R_X^s defined in the text. This model includes g_s but is valid for $d < \ell_m$ only since spin relaxation is disregarded. The interfaces lead to a saturation of η_s at short distances.

underestimate the experimental signal and, in contrast to experiments, deviate from the $\sim d^{-1}$ fit that might indicate an underestimated g_s. However, a larger g_s would lead to deviations at intermediate distances ($1 < d < 5\,\mu$m).

2. Spin transfer efficiency and equivalent circuit model

The spin transfer efficiency $\eta_s = \mu_s^{det}/\mu_s^{inj}$, i.e., the ratio between the spin accumulation in the injector and that in the detector, can be readily derived from the experiments by Eq. (20). From the voltage generated in the detector by the inverse spin Hall effect V_{ISHE} [48]

$$\mu_s^{det} = \frac{2t}{\theta L} \frac{1 + e^{-2t/\ell_s}}{(1 - e^{-t/\ell_s})^2} V_{ISHE}, \qquad (23)$$

where l is the length of the metal contact. The spin transfer efficiency therefore reads as

$$\eta_s = \frac{t}{\ell_s \theta^2} \frac{R_{nl}}{R_{det}} \frac{(e^{t/\ell_s} + 1)(e^{2t/\ell_s} + 1)}{(e^{t/\ell_s} - 1)^3}, \qquad (24)$$

where $R_{nl} = V_{ISHE}/I$ is the observed nonlocal resistance and R_{det} the detector resistance. Figure 8(a) shows the experimental data converted to the spin transfer efficiency as a function of distance d that is fitted to a 1D magnon spin diffusion model that does not include the interfaces [9]. When $d \rightarrow 0$ and interfaces are disregarded, η_s diverges. This artifact can be repaired by the equivalent spin-resistor circuit in Fig. 8(b)

according to which

$$\eta_s = \frac{R_{Pt}^s}{R_{YIG}^s + 2R_{int}^s + 2R_s^{Pt}}, \qquad (25)$$

where $R_{Pt}^s = \ell_s/[\sigma_e A_{int} \tanh(t/\ell_s)]$ is the spin resistance of the platinum strip [48], $R_{int}^s = 1/(g_s A_{int})$ is interface spin resistance, and $R_{YIG}^s = d/(\sigma_m A_{YIG})$ is the magnonic spin resistance of YIG. $A_{YIG} = l t_{YIG}$ is the cross section of the YIG channel and $A_{int} = wl$ is the area of the Pt|YIG interfaces. The parameters in Table II lead to the red dashed line in Fig. 8(a), which agrees well with the experimental data for $d < \ell_m$. No free parameters were used in this model since we adopted $\sigma_m = 5 \times 10^5$ S/m as extracted from our 2D model in the previous section.

The model predicts that the spin transfer efficiency should saturate for $d \lesssim 100$ nm for $g_s = 9.6 \times 10^{12}$ S/m^2. A predicted onset of saturation at 200 nm is not confirmed by the experiments, which as pointed out already in the previous section, could imply a larger g_s. Experiments on samples with even closer contacts are difficult but desirable. Based on the available data, we predict that the efficiency saturates at $\eta_s = 4 \times 10^{-3}$. The charge transfer efficiency (defined in Sec. III A 1) would be maximized at $\eta \approx 5 \times 10^{-5}$, which is still below the SMR $\Delta\rho/\rho = 2.6 \times 10^{-4}$, as predicted in Sec. III A 2.

3. Magnon temperature model

We can analyze the experiments also in terms of magnon temperature diffusion [1] as applied to the spin Seebeck [5,6] and spin Peltier [21] effects. Communication between the platinum injector and detector is possible via phonon and magnon heat transport: the spin accumulation at the injector can heat or cool the magnon/phonon system by the spin Peltier effect. The diffusive heat current generates a voltage at the detector by the spin Seebeck effect. However, pure phononic heat transport does not stroke with the exponential scaling, but decays only logarithmically (see below). The magnon temperature model (which describes the magnons in terms of their temperature only) can give an exponential scaling, but in order to agree with experiments, the magnon-phonon relaxation length must be large such that $T_m \neq T_p$ over large distances. This is at odds with the analysis by Schreier *et al.* and Flipse *et al.* However, we can test this model by, for the sake of argument, increasing this length scale by four orders of magnitude to $\ell_{mp} = 9.4\,\mu$m and completely disregard the magnon chemical potential. The spin Peltier heat current Q_{SPE}^{inj} is then [21]

$$Q_{SPE}^{inj} = L_s T \frac{\mu_s^{inj}}{2} A^{int}, \qquad (26)$$

where L_s is the interface spin Seebeck coefficient, $L_s = 2g^{\uparrow\downarrow}\gamma\hbar k_B/(eM_s\Lambda^3)$ [5,6,21], and $M_s = \mu_B S/a^3$ is the saturation magnetization of YIG. The equivalent circuit is based on the spin Peltier heat current and the spin thermal resistances of the YIG|Pt interfaces and the YIG channel. This allows us to find T_{m-e}, the temperature difference between magnons and electrons at the detector interface, which is the driving force for the SSE in this model. The equivalent thermal resistance circuit is shown in Fig. 9(b). Relaxation is disregarded, so
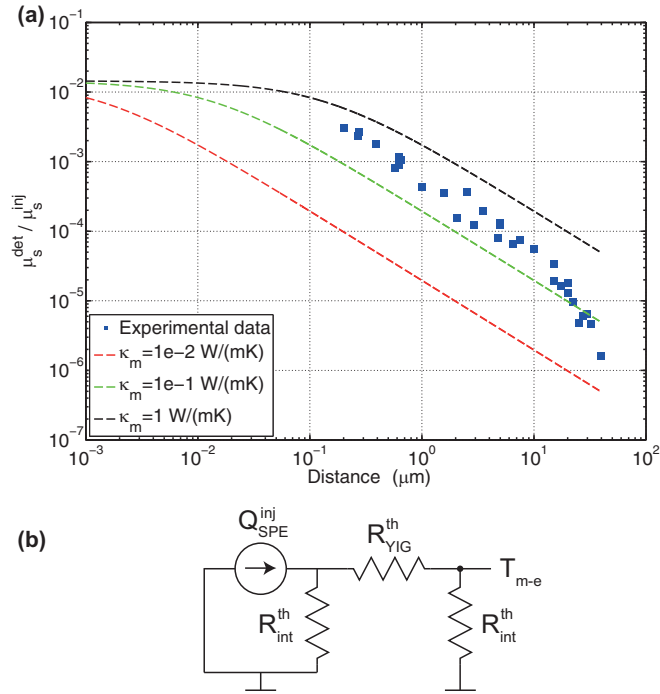
(a)

(b)

FIG. 9. (a) Results of the thermal model for $\kappa_m = 10^{-2}$ W/(mK) (red curve), $\kappa_m = 10^{-1}$ W/(mK) (green curve), and $\kappa_m = 1$ W/(mK) (black curve). Plotted on the y axis is the spin transfer efficiency resulting from the thermal model $\eta_{\rm th} = \mu_s^{\rm det}/\mu_s^{\rm inj}$. The blue squares represent the experimental data. (b) The equivalent thermal resistance model. The definitions of the thermal resistances used in the model are given in the main text. At the thermal grounds in the circuit, the temperature difference between magnons and electrons ($T_{\rm m-e}$) is zero.

the model is only valid for $d < \ell_{\rm mp}$. The interface magnetic heat resistance is given by $R_{\rm int}^{\rm th} = 1/(\kappa_s^I A_{\rm int})$, with κ_s^I equal to [5,6,21]

$$\kappa_s^I = \frac{h}{e^2}\frac{k_B T}{\hbar}\frac{\mu_B k_B g^{\uparrow\downarrow}}{\pi M_s \Lambda^3}, \qquad (27)$$

and where μ_B is the Bohr magneton. The YIG heat resistance $R_{\rm YIG}^{\rm th} = d/(\kappa_m A_{\rm YIG})$ and from the thermal circuit model we find that $T_{\rm m-e} = Q_{\rm SPE}^{\rm inj}(R_{\rm int}^{\rm th})^2/(R_{\rm int}^{\rm th} + R_{\rm YIG}^{\rm th})$, which generates a spin accumulation in the detector by the spin Seebeck effect

$$\mu_s^{\rm det} = T_{\rm m-e}\frac{g^{\uparrow\downarrow}\gamma\hbar k_B}{\pi M_s \Lambda^3}\frac{4\pi}{e}\frac{\ell_s}{\sigma}\tanh\left(\frac{t}{2\ell_s}\right)\frac{1+e^{-2t/\ell_s}}{(1-e^{-t/\ell_s})^2}. \qquad (28)$$

The thus obtained spin transfer efficiency $\eta_{\rm th}$ is plotted in Fig. 9(a) as a function of the magnon spin conductivity κ_m. For $\kappa_m \sim 0.1$–1 W/(mK) reasonable agreement with the experimental data can be achieved. While Schreier *et al.* argued that κ_m should be in the range 10^{-2}–10^{-3} W/(mK)), κ_m from Table I is also of the order of 1 W/(mK) at room temperature. Hence, the magnon temperature model can describe the nonlocal experiments, provided that the magnon-phonon relaxation length $\ell_{\rm mp}$ is large. However, from the expression for $\ell_{\rm mp}$ that we gave in Table I we find that $\ell_{\rm mp} \sim 10~\mu$m corresponds to $\tau_{\rm mp} \approx \tau_{\rm mr} \sim 1$ ns and $\kappa_m \sim 10^4$ W/(mK), which is at least three orders of magnitude larger than even the total YIG heat conductivity, and is clearly

unrealistic. Thus, requiring $\ell_{\rm mp} \sim 10~\mu$m while maintaining $\kappa_m \sim 1$ W/(mK) is inconsistent. Also, an $\ell_{\rm mp}$ of the order of nanometers as reported by Schreier *et al.* and Flipse *et al.* is difficult to reconcile with the observed length scale of the order of $10~\mu$m.

Up to now, we disregarded phononic heat transport. As argued, the interaction of phonons with magnons in the spin channel is weak, but the energy transfer can be efficient. The spin Peltier effect at the contact generates a magnon heat current that decays on the length scale $\ell_{\rm mp}$, heating up the phonons that subsequently diffuse to the detector, where they cause a spin Seebeck effect. The magnon system is in equilibrium except at distances from injector and detector on the scale $\ell_{\rm mp}$ that we argued to be short. In this scenario, there is no nonlocal magnon transport in the bulk at all, but injector and detector communicate by pure phonon heat transport. However, this mechanism does not explain the exponential decay of the nonlocal signal: the diffusive heat current emitted by a line source, taking into account that the gadolinium gallium garnet (GGG) substrate has a heat conductivity close to that of YIG [6], decays only logarithmically as a function of distance.

D. Longitudinal spin Seebeck effect

The spin Seebeck effect is usually measured in the longitudinal configuration, i.e., samples with a YIG film grown on GGG and a Pt top contact. Longitudinal spin Seebeck measurements are hence local measurements, as opposed to the nonlocal experiments we have discussed in the preceding sections. However, in the longitudinal configuration our one-dimensional model [17] is still applicable. A recent study extracted the length scale of the longitudinal spin Seebeck effect from experiments on samples with various YIG film thicknesses [49]. A length of the order of 1 μm was found. Similar results were obtained by Kikkawa *et al.* [50].

We assume a constant gradient $(T_L - T_R)/d < 0$, where T_L, T_R are the temperatures at the interfaces of YIG to GGG, platinum, respectively, with T_m everywhere equilibrized to T_p, and disregard the Kapitza heat resistance [cf. Fig. 10(a)]. At the YIG|GGG interface the spin current vanishes. Figure 10 illustrates the magnon chemical potential profile on the YIG thickness d as well as the transparency of the Pt|YIG interface for four limiting cases, i.e., for opaque ($g_s < \sigma_m/\ell_m$) and transparent ($g_s > \sigma_m/\ell_m$) interfaces and a thick ($d > \ell_m$) and a thin ($d < \ell_m$) YIG film, in which analytic results can be derived.

We define a spin Seebeck coefficient as the normalized inverse spin Hall voltage $V_{\rm ISHE}/t_y$ in the platinum film of length t_y divided by the temperature gradient $\Delta T/d$, with $\Delta T = T_L - T_R$ and average temperature T_0:

$$\sigma_{\rm SSE} = \frac{d V_{\rm ISHE}}{t_y \Delta T}. \qquad (29)$$

Assuming that the Pt spin diffusion length ℓ_s is much shorter than its film thickness t, we find the analytic expression

$$\sigma_{\rm SSE} = \frac{g_s \ell_s \ell_m L\theta\left[\cosh\frac{d}{\ell_m} - 1\right]}{t\sigma_e T_0\left[g_s\ell_m\cosh\frac{d}{\ell_m} + \sigma_m\left(1 + \frac{2g_s\ell_s}{\sigma_e}\right)\sinh\frac{d}{\ell_m}\right]}. \qquad (30)$$
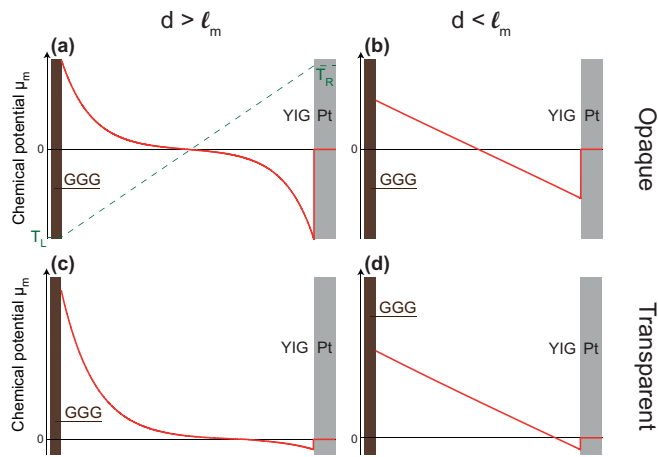
FIG. 10. Magnon chemical potential μ_m under the spin Seebeck effect for a linear temperature gradient in YIG, in the limit of (a) an opaque interface and thick YIG, (b) an opaque interface and thin YIG, (c) a transparent interface and thick YIG, and (d) a transparent interface and thin YIG. In all four cases, μ_m changes sign somewhere in the YIG. For higher interface transparency (larger g_s), the zero crossing shifts closer to the Pt|YIG interface.

In Fig. 11, σ_{SSE} is plotted as a function of the relative thickness d/ℓ_m of the magnetic insulator in the transport direction, Pt thickness of $t = 10$ nm and $T_0 = 300$ K. We adopt L from Table I and a relaxation time $\tau \sim \tau_{\mathrm{mp}} \sim 0.1$ ps and the parameters from Fig. 11. The normalized spin Seebeck coefficient saturates as a function of d on the scale of the magnon spin diffusion length ℓ_m. While experiments at $T_0 \leqslant 250$ K report somewhat smaller length scales than our ℓ_m, our saturation $\sigma_{\mathrm{SSE}} \sim 0.1$–$1$ μV/K is of the same order as the experiments [51].

In the limit of an opaque interface, σ_{SSE} saturates to

$$\sigma_{\mathrm{SSE}}(d \gg \ell_m) = \frac{g_s \ell_s \ell_m L\theta}{t T_0 \sigma_e \sigma_m} = \left(\frac{g_s \ell_s}{\sigma_e}\right)\left(\frac{\ell_m}{t}\right)\frac{\alpha_\mu \theta k_B}{e}, \quad (31)$$

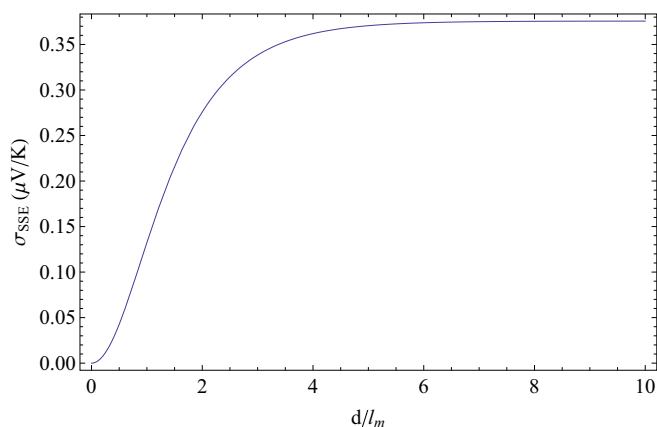in terms of the dimensionless ratio α_μ from Eq. (7).

FIG. 11. Normalized spin Seebeck coefficient as a function of the thickness of the magnetic insulator in the direction of the temperature gradient. Parameters taken are from Table II, together with a Pt thickness of $t = 10$ nm and temperature of 300 K. The value for the bulk spin Seebeck coefficient L is taken from the expression in Table I with $\tau = 0.1$ ps.

For a transparent interface with $\ell_m \gg \ell_s$ and $\sigma_m \sim \sigma_e$, the result is governed by bulk parameters only:

$$\sigma_{\mathrm{SSE}}(d \to \infty) = \frac{\ell_s L\theta}{t T_0 \sigma_e}. \quad (32)$$

This model for the spin Seebeck effect is oversimplified by assuming a vanishing magnon-phonon relaxation length and disregarding interface heat resistances. The gradient in the phonon temperature can give rise to a spin Seebeck voltage [52] even when bulk magnon spin transport is frozen out by a large magnetic field. Nevertheless, it is remarkable that it gives a reasonable qualitative description for the spin Seebeck effect with input parameters adapted for electrically driven magnon transport. We conclude that also in the description of the spin Seebeck effect the magnon chemical potential can play a crucial role.

IV. CONCLUSIONS

We presented a diffusion theory for magnon spin and heat transport in magnetic insulators actuated by metallic contacts. In contrast to previous models, we focus on the magnon chemical potential. This is an essential ingredient because under ambient conditions $\ell_m > \ell_{\mathrm{mp}}$, i.e., the magnon chemical potential relaxes over much larger length scales than the magnon temperature. We compare theoretical results for electrical magnon injection and detection with nonlocal transport experiments on YIG|Pt structures [9], for both a 1D analytical and a 2D finite-element model.

In the 1D model, we study the relevance of interface versus bulk-limited transport and find that, for the materials and conditions considered, the interface spin resistance dominates. For the limiting cases of transparent and opaque interfaces, the spin transfer efficiency η decays algebraically $\propto 1/d$ as a function of injector-detector distance d when $d < \ell_m$, and exponentially with a characteristic length ℓ_m for $d > \ell_m$.

A 2D finite-element model for the actual sample configurations can be fitted well to the experiments for different contact distances, leading to a magnon conductivity $\sigma_m = 5 \times 10^5$ S/m and diffusion length $\ell_m = 9.4$ μm.

The experiments measure first- and second-order harmonic signals that are attributed to electrical magnon spin injection/detection and thermal generation of magnons by Joule heating with spin Seebeck effect detection, respectively. Here, we focus on the linear response that we argue to be dominated by the diffusion of a magnon accumulation governed by the chemical potential, rather than the magnon temperature. However, we applied our theory also to the standard longitudinal (local) spin Seebeck geometry. We find the same length scale ℓ_m and a (normalized) spin Seebeck coefficient of $\sigma_{\mathrm{SSE}} \sim 0.1$–$1$ μV/K for $d \gg \ell_m$, which is of the same order of magnitude as the observations [49].

APPENDIX: BOLTZMANN TRANSPORT THEORY

Here, we derive our magnon transport theory from the linearized Boltzmann equation in the relaxation time approximation, thereby introducing and estimating the different collision times.

1. Boltzmann equation

Equations (5)–(7) are based on the Boltzmann equation for the magnon distribution function $f(\mathbf{x},\mathbf{k},t)$:

$$\frac{\partial f}{\partial t} + \frac{\partial f}{\partial \mathbf{x}} \cdot \frac{\partial \omega_{\mathbf{k}}}{\partial \mathbf{k}} = \Gamma^{\text{in}}[f] - \Gamma^{\text{out}}[f], \quad (A1)$$

where $\Gamma^{\text{in}} = \Gamma^{\text{in}}_{\text{el}} + \Gamma^{\text{in}}_{\text{mr}} + \Gamma^{\text{in}}_{\text{mp}} + \Gamma^{\text{in}}_{\text{mm}}$ and $\Gamma^{\text{out}} = \Gamma^{\text{out}}_{\text{el}} + \Gamma^{\text{out}}_{\text{mr}} + \Gamma^{\text{out}}_{\text{mp}} + \Gamma^{\text{out}}_{\text{mm}}$ are the total rates of scattering into and out of a magnon state with wave vector $\mathbf{k}$, respectively. The subscripts refer to elastic magnon scattering at defects, magnon relaxation by magnon-phonon interactions that do not conserve magnon number, magnon-conserving inelastic and elastic magnon-phonon interactions, and magnon number and energy-conserving magnon-magnon interactions. We discuss them in the following for an isotropic magnetic insulator and in the limit of small magnon and phonon numbers.

The elastic magnon scattering is given by Fermi's golden rule as

$$\Gamma^{\text{out}}_{\text{el}} = \frac{2\pi}{\hbar} \sum_{\mathbf{k}'} \left| V^{\text{el}}_{\mathbf{k}\mathbf{k}'} \right|^2 \delta(\hbar\omega_{\mathbf{k}} - \hbar\omega_{\mathbf{k}'}) f(\mathbf{k},t), \quad (A2)$$

where $V^{\text{el}}_{\mathbf{k}\mathbf{k}'}$ is the matrix element for scattering by defects and rough boundaries [23,37] of a magnon with momentum $\hbar\mathbf{k}$ to one with $\hbar\mathbf{k}'$ at the same energy. $\Gamma^{\text{in}}_{\text{el}}$ is obtained from this expression by interchanging $\mathbf{k}$ and $\mathbf{k}'$. In the presence of the in-scattering term (vertex correction) $\Gamma^{\text{in}}_{\text{el}}$, the Boltzmann equation is an integrodifferential rather than a simple differential equation.

Gilbert damping parametrizes the magnon dissipation into the phonon bath. According to the linearized Landau-Lifshitz-Gilbert equation [32]

$$\Gamma^{\text{out}}_{\text{mr}} = 2\alpha_G \omega_{\mathbf{k}} f(\mathbf{k},t). \quad (A3)$$

Since the phonons are assumed to be at thermal equilibrium with temperature T_p, $\Gamma^{\text{in}}_{\text{mr}}$ is obtained by substituting $f(\mathbf{k},t) \to n_B(\hbar\omega_{\mathbf{k}}/k_B T_p)$ in $\Gamma^{\text{out}}_{\text{mr}}$.

Magnon-conserving magnon-phonon interactions with matrix elements $V^{\text{mp}}_{\mathbf{k}\mathbf{k}'\mathbf{q}}$ generate the out-scattering rate

$$\Gamma^{\text{out}}_{\text{mp}} = \frac{2\pi}{\hbar} \sum_{\mathbf{k}',\mathbf{q}} \left| V^{\text{mp}}_{\mathbf{k}\mathbf{k}'\mathbf{q}} \right|^2 \delta(\hbar\omega_{\mathbf{k}} - \hbar\omega_{\mathbf{k}'} - \epsilon_{\mathbf{q}})$$

$$\times f(\mathbf{k},t)[(1 + f(\mathbf{k}',t)]\left[1 + n_B\left(\frac{\epsilon_{\mathbf{q}}}{k_B T_p}\right)\right], \quad (A4)$$

where $\epsilon_{\mathbf{q}} = \hbar c|\mathbf{q}|$ is the acoustic phonon dispersion with sound velocity c and momentum $\mathbf{q}$. The "in" scattering rate

$$\Gamma^{\text{in}}_{\text{mp}} = \frac{2\pi}{\hbar} \sum_{\mathbf{k}',\mathbf{q}} \left| V^{\text{mp}}_{\mathbf{k}\mathbf{k}'\mathbf{q}} \right|^2 \delta(\hbar\omega_{\mathbf{k}} - \hbar\omega_{\mathbf{k}'} - \epsilon_{\mathbf{q}})$$

$$\times f(\mathbf{k}',t)[(1 + f(\mathbf{k},t)]n_B\left(\frac{\epsilon_{\mathbf{q}}}{k_B T_p}\right). \quad (A5)$$

Finally, the four-magnon interactions (two magnons in, two magnons out) generate

$$\Gamma^{\text{out}}_{\text{mm}} = \frac{2\pi}{\hbar} \sum_{\mathbf{k}',\mathbf{k}'',\mathbf{k}'''} \left| V^{\text{mm}}_{\mathbf{k}+\mathbf{k}',\mathbf{k}-\mathbf{k}',\mathbf{k}''-\mathbf{k}'''} \right|^2$$

$$\times \delta(\hbar\omega_{\mathbf{k}} + \hbar\omega_{\mathbf{k}'} - \hbar\omega_{\mathbf{k}''} - \hbar\omega_{\mathbf{k}'''})\delta(\mathbf{k} + \mathbf{k}' - \mathbf{k}'' - \mathbf{k}''')$$

$$\times f(\mathbf{k},t)f(\mathbf{k}',t)[1 + f(\mathbf{k}'',t)][1 + f(\mathbf{k}''',t)], \quad (A6)$$

while $\Gamma^{\text{in}}_{\text{mm}}$ follows by exchanging $\mathbf{k}\mathbf{k}''$, and $\mathbf{k}'$ and $\mathbf{k}'''$. Disregarding umklapp scattering, the magnon-magnon interactions conserve linear and angular momentum. V^{mm} therefore depends only on the center-of-mass momentum and the relative magnon momenta before and after the collision, which implies that Γ_{mm} does not affect transport directly (analogous to the role of electron-electron interactions in electric conduction).

The collision rates govern the energy and momentum-dependent collision times $\tau_a(k,\hbar\omega)$ (with $a \in \{\text{el},\text{mr},\text{mp},\text{mm}\}$). These are defined from the "out" rates via

$$\frac{1}{\tau_a(k,\hbar\omega)} = \frac{\Gamma^{\text{out}}_a}{f(\mathbf{k},t)}, \quad (A7)$$

replacing $f \to n_B(\hbar\omega_{\mathbf{k}}/k_B T_p)$ and $\hbar\omega_{\mathbf{k}}$ with $\hbar\omega$ where phonons are involved. Here, we are interested mainly in thermal magnons for which the relevant collision times are evaluated at energy $\hbar\omega = k_B T$ and momentum $k = \Lambda^{-1}$. Then, $1/\tau_{\text{mr}} \sim \alpha_G k_B T/\hbar$. Elastic magnon scattering can be parametrized by a mean-free path $\ell_{\text{el}} = \tau_{\text{el}}(k,\hbar\omega)\partial\omega_{\mathbf{k}}/\partial k$, and therefore $1/\tau_{\text{el}}(k,\hbar\omega) = 2\ell_{\text{el}}^{-1}\sqrt{J_s\omega/\hbar}$ or $\tau_{\text{el}} = \ell_{\text{el}}/v_{\text{m}}$, where $v_{\text{m}} = 2\sqrt{J_s\omega/\hbar}$ is the magnon group velocity. Estimates for ℓ_{el} range from 1 μm [23] under the assumption that ℓ_{el} is due to Gilbert damping and disorder only, to 500 μm [37]. Therefore, $\tau_{\text{el}} \sim 10$–10^5 ps. Since we deduce in the main text that at room temperature τ_{mp} is one to two orders of magnitude smaller than this τ_{el}, we completely disregard elastic two-magnon scattering in the comparison with experiments.

We adopt the relaxation time approximation in which the scattering terms read as

$$\Gamma[f] = \frac{1}{\tau_{\text{el}}}\left[f - n_B\left(\frac{\hbar\omega_{\mathbf{k}} - \mu_m}{k_B T_m}\right) \right]$$

$$+ \frac{1}{\tau_{\text{mr}}}\left[f - n_B\left(\frac{\hbar\omega_{\mathbf{k}}}{k_B T_p}\right) \right]$$

$$+ \frac{1}{\tau_{\text{mp}}}\left[f - n_B\left(\frac{\hbar\omega_{\mathbf{k}} - \mu_m}{k_B T_p}\right) \right]$$

$$+ \frac{1}{\tau_{\text{mm}}}\left[f - n_B\left(\frac{\hbar\omega_{\mathbf{k}} - \mu_m}{k_B T_m}\right) \right]. \quad (A8)$$

The distribution functions here are chosen such that the elastic scattering processes stop when f approaches the Bose-Einstein distribution with local chemical potential $\mu_m \neq 0$,

in contrast to the inelastic scattering that causes relaxation to thermal equilibrium with the lattice and $\mu_m = 0$. Similarly, the temperatures T_p vs T_m are chosen to express that the scattering exchanges energy with the phonons or keeps it in the magnon system, respectively.

The Boltzmann equation may be linearized in terms of the small perturbations, i.e., the gradients of temperature and chemical potential. The local momentum space shift δf of the magnon distribution function

$$\delta f(\mathbf{x},\mathbf{k}) = \tau \frac{\partial n_B\left(\frac{\hbar\omega_{\mathbf{k}}}{k_B T_p}\right)}{\partial \hbar\omega_{\mathbf{k}}} \frac{\partial \omega_{\mathbf{k}}}{\partial \mathbf{k}} \cdot \left(\nabla_{\mathbf{x}}\mu_m + \hbar\omega_{\mathbf{k}}\frac{\nabla_{\mathbf{x}} T_m}{T_p}\right), \tag{A9}$$

where $1/\tau = 1/\tau_{mr} + 1/\tau_{mp}$. The magnon spin and heat currents [Eq. (5)] are obtained by substituting δf into

$$\mathbf{j}_m = \hbar \int \frac{d\mathbf{k}}{(2\pi)^3} \delta f(\mathbf{k}) \frac{\partial \omega_{\mathbf{k}}}{\partial \mathbf{k}}, \tag{A10}$$

$$\mathbf{j}_{Q,m} = \int \frac{d\mathbf{k}}{(2\pi)^3} \delta f(\mathbf{k}) \hbar\omega_{\mathbf{k}} \frac{\partial \omega_{\mathbf{k}}}{\partial \mathbf{k}}. \tag{A11}$$

The magnon spin and heat diffusion [Eq. (6)] are obtained by a momentum integral of the Boltzmann equation (A8) after multiplying by $\hbar$ and $\hbar\omega_{\mathbf{k}}$, respectively. The local distribution function in the collision terms consists of the sum of the "drift" term δf and the Bose-Einstein distribution with local temperature and chemical potential

$$f(\mathbf{k},t) = \delta f + n_B([\hbar\omega_{\mathbf{k}} - \mu_m(\mathbf{x})]/[k_B T_m(\mathbf{x})]). \tag{A12}$$

We reiterate that the relatively efficient magnon conserving τ_m limits the energy, but not (directly) the spin diffusion.

2. Magnon-magnon scattering rate

The four-magnon scattering rate is believed to efficiently thermalize the local magnon distribution to the Bose-Einstein form [31,32]. At room temperature, the leading-order correction to the exchange interaction in the presence of magnetization textures reads as

$$H_{\mathrm{xc}} = -\frac{J_s}{2s} \int d\mathbf{x}\, \mathbf{s}(\mathbf{x}) \cdot \nabla^2 \mathbf{s}(\mathbf{x}), \tag{A13}$$

where $\mathbf{s}(\mathbf{x})$ ($s = |\mathbf{s}| = S/a^3$) is the spin density. By the Holstein-Primakoff transformation, the spin-lowering operator reads as $\hat{s}_- = s_x - i s_y = \sqrt{2s - \hat{\psi}^\dagger\hat{\psi}}\,\hat{\psi} \simeq \sqrt{2s}\,\hat{\psi} - \hat{\psi}^\dagger\hat{\psi}\hat{\psi}/2\sqrt{2s}$ in terms of the bosonic creation ($\hat{\psi}^\dagger$) and annihilation ($\hat{\psi}$) operators. H_{xc} can be approximated as a four-particle pointlike interaction term

$$H_{\mathrm{mm}} \approx g \int d\mathbf{x}\, \hat{\psi}^\dagger\hat{\psi}^\dagger\hat{\psi}\hat{\psi}, \tag{A14}$$

where $g \sim k_B T/s$ is the exchange interaction strength at thermal energies. Using Fermi's golden rule for this interaction yields collision terms as Eq. (A6) with $V^{mm} \approx g$:

$$\frac{1}{\tau_{\mathrm{mm}}(k,\hbar\omega)} \approx \frac{g^2}{\hbar} \sum_{\mathbf{k}',\mathbf{k}'',\mathbf{k}'''} \delta(\hbar\omega_{\mathbf{k}} + \hbar\omega_{\mathbf{k}'} - \hbar\omega_{\mathbf{k}''} - \hbar\omega_{\mathbf{k}'''})\delta(\mathbf{k} + \mathbf{k}' - \mathbf{k}'' - \mathbf{k}''') \times n_B\left(\frac{\hbar\omega_{\mathbf{k}'}}{k_B T_p}\right)$$

$$\times \left[1 + n_B\left(\frac{\hbar\omega_{\mathbf{k}''}}{k_B T_p}\right)\right]\left[1 + n_B\left(\frac{\hbar\omega_{\mathbf{k}'''}}{k_B T_p}\right)\right]. \tag{A15}$$

The momentum integrals can be estimated for thermal magnons with $k = \Lambda^{-1}$ and $\hbar\omega = k_B T$ and

$$\frac{1}{\tau_{\mathrm{mm}}} \approx \frac{g^2}{\Lambda^6} \frac{k_B T}{\hbar} \approx \left(\frac{T}{T_c}\right)^3 \frac{k_B T}{\hbar}, \tag{A16}$$

with Curie temperature $k_B T_c \approx J_s s^{2/3}$. With parameters for YIG $J_s s^{2/3}/k_B \approx 200$ K, which is the correct order of magnitude. The T^4 scaling of the four-magnon interaction rate results from the combined effects of the magnon density of states (magnon scattering phase space) and energy dependence of the exchange interactions.

While the magnon-magnon scattering is efficient at thermal energies, it becomes slow at low energies close to the band edge due to phase space restrictions and leads to deviations from the Bose-Einstein distribution functions that may be disregarded at room temperature.

3. Magnon-conserving magnon-phonon interactions

At thermal energies and large wave numbers, the magnon-conserving magnon-phonon scattering [37] is dominated by

the dependence of the exchange interaction on lattice distortions rather than magnetocrystalline fields. Since we estimate orders of magnitude, we disregard phonon polarization and the tensor character of the magnetoelastic interaction and start from the Hamiltonian

$$H_{\mathrm{mp}} = -\frac{B}{s} \int d\mathbf{x}\, \mathbf{s}(\mathbf{x}) \cdot \nabla^2 \mathbf{s}(\mathbf{x}) \left(\sum_{\alpha \in \{x,y,z\}} \frac{\partial R}{\partial x_\alpha}\right), \tag{A17}$$

where B is a magnetoelastic constant. The scalar lattice displacement field R can be expressed in the phonon creation and annihilation operators $\hat{\phi}^\dagger$ and $\hat{\phi}$ as

$$R = \sqrt{\frac{\hbar^2}{2\rho\epsilon}}[\hat{\phi} + \hat{\phi}^\dagger], \tag{A18}$$

where ϵ is the phonon energy and ρ the mass density. By the Holstein-Primakoff transformation introduced in the previous

section, we find to leading order

$$H_{\mathrm{mp}} \approx B \int dx (\nabla \hat{\psi}^{\dagger}) \cdot (\nabla \hat{\psi}) \left(\frac{\hbar^2}{\rho \epsilon} \right) \left(\sum_{\alpha \in \{x,y,z\}} \frac{\partial \hat{\phi}}{\partial x_\alpha} \right) + \text{H.c.}$$
(A19)

This Hamiltonian is the scattering potential in the matrix elements of Eq. (A5):

$$\left| V_{\mathbf{k}\mathbf{k}'\mathbf{q}}^{\mathrm{mp}} \right|^2 \approx \frac{B^2 \hbar^2 q^2}{\rho \epsilon_{\mathbf{q}}} (\mathbf{k} \cdot \mathbf{k}')^2 \delta(\mathbf{k} - \mathbf{k}' - \mathbf{q})$$
(A20)

which by substitution and in the limit $\Lambda \ll \Lambda_p$, where $\Lambda_p = \hbar c / k_B T_p$ is the phonon thermal de Broglie wavelength, leads to

$$\frac{1}{\tau_{\mathrm{mp}}} \sim \frac{B^2}{\hbar \rho} \left(\frac{\hbar}{k_B T} \right)^2 \frac{1}{\Lambda^4 \Lambda_p^5}.$$
(A21)

In the opposite limit $\Lambda \gg \Lambda_p$,

$$\frac{1}{\tau_{\mathrm{mp}}} \sim \frac{B^2}{\hbar \rho} \left(\frac{\hbar}{k_B T} \right)^2 \frac{1}{\Lambda^7 \Lambda_p^2}.$$
(A22)

At room temperature $\Lambda \approx \Lambda_p$ and for $\rho a^3 = 10^{-24}$ kg both expressions lead to $\tau_{\mathrm{mp}} = 10 (J_s/B)^2$ ns [38]. We could not find estimates of B for YIG in the literature. In iron, exchange interactions change by a factor of 2 upon small lattice distortion $\Delta a \ll a$ [53]. While the authors of this latter work find that this does not strongly affect the Curie temperature, it leads to fast magnon-phonon scattering as we show now. Namely, $B \sim a \partial J_s / \partial \Delta a |_{\Delta a = 0} \approx a J_s / \Delta a$, so that $\tau_{\mathrm{mp}} = 10 (\Delta a/a)^2$ ns, which is many orders of magnitude smaller than one ns (and thus smaller than τ_{mr} at room temperature). While no proof, this argument supports our hypothesis that the magnon temperature relaxation length is much shorter than that of the magnon chemical potential.

[1] D. Sanders and D. Walton, Phys. Rev. B **15**, 1489 (1977).

[2] K. Uchida, J. Xiao, H. Adachi, J. Ohe, S. Takahashi, J. Ieda, T. Ota, Y. Kajiwara, H. Umezawa, H. Kawai, G. E. W. Bauer, S. Maekawa, and E. Saitoh, Nat. Mater. **9**, 894 (2010).

[3] G. E. W. Bauer, E. Saitoh, and B. J. van Wees, Nat. Mater. **11**, 391 (2012).

[4] H. Adachi, K.-i. Uchida, E. Saitoh, and S. Maekawa, Rep. Prog. Phys. **76**, 36501 (2013).

[5] J. Xiao, G. E. W. Bauer, K.-i. Uchida, E. Saitoh, and S. Maekawa, Phys. Rev. B **81**, 214418 (2010).

[6] M. Schreier, A. Kamra, M. Weiler, J. Xiao, G. E. W. Bauer, R. Gross, and S. T. B. Goennenwein, Phys. Rev. B **88**, 094410 (2013).

[7] S. M. Rezende, R. L. Rodríguez-Suárez, R. O. Cunha, A. R. Rodrigues, F. L. A. Machado, G. A. Fonseca Guerra, J. C. Lopez Ortiz, and A. Azevedo, Phys. Rev. B **89**, 014416 (2014).

[8] S. Hoffman, K. Sato, and Y. Tserkovnyak, Phys. Rev. B **88**, 064408 (2013).

[9] L. J. Cornelissen, J. Liu, R. A. Duine, J. Ben Youssef, and B. J. van Wees, Nat. Phys. **11**, 1022 (2015).

[10] S. T. B. Goennenwein, R. Schlitz, M. Pernpeintner, K. Ganzhorn, M. Althammer, R. Gross, and H. Huebl, Appl. Phys. Lett. **107**, 172405 (2015).

[11] B. L. Giles, Z. Yang, J. S. Jamison, and R. C. Myers, Phys. Rev. B **92**, 224415 (2015).

[12] H. Wu, C. H. Wan, X. Zhang, Z. H. Yuan, Q. T. Zhang, J. Y. Qin, H. X. Wei, X. F. Han, and S. Zhang, Phys. Rev. B **93**, 060403 (2016).

[13] J. Li, Y. Xu, M. Aldosary, C. Tang, Z. Lin, S. Zhang, R. Lake, and J. Shi, Nat. Commun. **7**, 10858 (2016).

[14] A. A. Serga, A. V. Chumak, and B. Hillebrands, J. Phys. D: Appl. Phys. **43**, 264002 (2010).

[15] A. Rückriegel and P. Kopietz, Phys. Rev. Lett. **115**, 157203 (2015).

[16] S. O. Demokritov, V. E. Demidov, O. Dzyapko, G. A. Melkov, A. A. Serga, B. Hillebrands, and A. N. Slavin, Nature (London) **443**, 430 (2006).

[17] R. A. Duine, A. Brataas, S. A. Bender, and Y. Tserkovnyak, arXiv:1505.01329v1.

[18] I. Zutic, J. Fabian, and S. D. Sarma, Rev. Mod. Phys. **76**, 323 (2004).

[19] F. K. Dejene, J. Flipse, G. E. W. Bauer, and B. J. van Wees, Nat. Phys. **9**, 636 (2013).

[20] S. S.-L. Zhang and S. Zhang, Phys. Rev. Lett. **109**, 096603 (2012).

[21] J. Flipse, F. K. Dejene, D. Wagenaar, G. E. W. Bauer, J. B. Youssef, and B. J. van Wees, Phys. Rev. Lett. **113**, 027601 (2014).

[22] S. R. Boona and J. P. Heremans, Phys. Rev. B **90**, 064421 (2014).

[23] B. Flebus, S. A. Bender, Y. Tserkovnyak, and R. A. Duine, Phys. Rev. Lett. **116**, 117201 (2016).

[24] D. G. Cahill, W. K. Ford, K. E. Goodson, G. D. Mahan, A. Majumdar, H. J. Maris, R. Merlin, and S. R. Phillpot, J. Appl. Phys. **93**, 793 (2003).

[25] L. Wang, R. J. H. Wesselink, Y. Liu, Z. Yuan, K. Xia, and P. J. Kelly, Phys. Rev. Lett. **116**, 196602 (2016).

[26] Y.-T. Chen, S. Takahashi, H. Nakayama, M. Althammer, S. T. B. Goennenwein, E. Saitoh, and G. E. W. Bauer, J. Phys.: Condens. Matter **28**, 103004 (2016).

[27] Y. Tserkovnyak and S. A. Bender, Phys. Rev. B **90**, 014428 (2014).

[28] M. B. Lifshits and M. I. Dyakonov, Phys. Rev. Lett. **103**, 186601 (2009).

[29] M. Weiler, M. Althammer, M. Schreier, J. Lotze, M. Pernpeintner, S. Meyer, H. Huebl, R. Gross, A. Kamra, J. Xiao, Y.-T. Chen, H. J. Jiao, G. E. W. Bauer, and S. T. B. Goennenwein, Phys. Rev. Lett. **111**, 176601 (2013).

[30] M. Isasa, E. Villamor, L. E. Hueso, M. Gradhand, and F. Casanova, Phys. Rev. B **91**, 024402 (2015).

[31] F. J. Dyson, Phys. Rev. **102**, 1217 (1956).

[32] S. A. Bender, R. A. Duine, A. Brataas, and Y. Tserkovnyak, Phys. Rev. B **90**, 094409 (2014).

[33] T. Gilbert, IEEE Trans. Magn. **40**, 3443 (2004).

[34] S. A. Bender, R. A. Duine, and Y. Tserkovnyak, Phys. Rev. Lett. **108**, 246601 (2012).

[35] S. A. Bender and Y. Tserkovnyak, Phys. Rev. B **91**, 140402 (2015).

[36] J. Xiao and G. E. W. Bauer, arXiv:1508.02486.

[37] C. M. Bhandari and G. S. Verma, Phys. Rev. **152**, 731 (1966).

[38] A. Rückriegel, P. Kopietz, D. A. Bozhko, A. A. Serga, and B. Hillebrands, Phys. Rev. B **89**, 184413 (2014).

[39] V. Cherepanov, I. Kolokolov, and V. L'Vov, Phys. Rep. **229**, 81 (1993).

[40] M.-H. Nguyen, D. C. Ralph, and R. A. Buhrman, Phys. Rev. Lett. **116**, 126601 (2016).

[41] H. Nakayama, M. Althammer, Y.-T. Chen, K. Uchida, Y. Kajiwara, D. Kikuchi, T. Ohtani, S. Geprägs, M. Opel, S. Takahashi, R. Gross, G. E. W. Bauer, S. T. B. Goennenwein, and E. Saitoh, Phys. Rev. Lett. **110**, 206601 (2013).

[42] N. Vlietstra, J. Shan, V. Castel, B. J. van Wees, and J. Ben Youssef, Phys. Rev. B **87**, 184421 (2013).

[43] Y.-T. Chen, S. Takahashi, H. Nakayama, M. Althammer, S. T. B. Goennenwein, E. Saitoh, and G. E. W. Bauer, Phys. Rev. B **87**, 144411 (2013).

[44] M. B. Jungfleisch, V. Lauer, R. Neb, A. V. Chumak, and B. Hillebrands, Appl. Phys. Lett. **103**, 022411 (2013).

[45] K.-i. Uchida, Z. Qiu, T. Kikkawa, R. Iguchi, and E. Saitoh, Appl. Phys. Lett. **106**, 052405 (2015).

[46] S. Meyer, M. Althammer, S. Geprägs, M. Opel, R. Gross, and S. T. B. Goennenwein, Appl. Phys. Lett. **104**, 242411 (2014).

[47] A. Slachter, F. L. Bakker, and B. J. van Wees, Phys. Rev. B **84**, 174408 (2011).

[48] V. Castel, N. Vlietstra, J. Ben Youssef, and B. J. van Wees, Appl. Phys. Lett. **101**, 132414 (2012).

[49] A. Kehlberger, U. Ritzmann, D. Hinzke, E.-J. Guo, J. Cramer, G. Jakob, M. C. Onbasli, D. H. Kim, C. A. Ross, M. B. Jungfleisch, B. Hillebrands, U. Nowak, and M. Kläui, Phys. Rev. Lett. **115**, 096602 (2015).

[50] T. Kikkawa, K.-i. Uchida, S. Daimon, Z. Qiu, Y. Shiomi, and E. Saitoh, Phys. Rev. B **92**, 064413 (2015).

[51] E.-J. Guo, A. Kehlberger, J. Cramer, G. Jakob, and M. Kläui, arXiv:1506.06037.

[52] L. J. Cornelissen and B. J. van Wees, Phys. Rev. B **93**, 020403(R) (2016).

[53] R. F. Sabiryanov and S. S. Jaswal, Phys. Rev. Lett. **83**, 2062 (1999).